

DEUTERIUM TOWARD TWO MILKY WAY DISK STARS: PROBING EXTENDED SIGHT LINES WITH THE FAR ULTRAVIOLET SPECTROSCOPIC EXPLORER

CHARLES G. HOOPES¹, KENNETH R. SEMBACH², GUILLAUME HÉBRARD³, H. WARREN MOOS¹,
AND DAVID C. KNAUTH¹
Draft version October 31, 2018

ABSTRACT

We have carried out an investigation of the abundance of deuterium along two extended sight lines through the interstellar medium (ISM) of the Galactic disk. The data include *Far Ultraviolet Spectroscopic Explorer (FUSE)* observations of HD 195965 (B1Ib) and HD 191877 (B0V), as well as Space Telescope Imaging Spectrograph (STIS) observations of HD 195965. The distances to HD 195965 and HD 191877, derived from spectroscopic parallax, are 794 ± 200 pc and 2200 ± 550 pc, respectively, making these the longest Galactic disk sight lines in which deuterium has been investigated with *FUSE*. The *FUSE* spectra contain all of the H I Lyman series transitions (and the corresponding D transitions) except Ly α . The higher Lyman lines clearly show the presence of deuterium. We use a combination of curve of growth analyses and line profile fitting to determine the D I abundance toward each object. We also present column densities for O I and N I toward both stars, and H I measured from Ly α absorption in the STIS spectrum of HD 195965. Toward HD 195965 we find $D/H = (0.85 \pm_{0.24}^{0.34}) \times 10^{-5}$ (2σ), $O/H = (6.61 \pm_{1.11}^{1.03}) \times 10^{-4}$, and $N/H = (7.94 \pm_{1.34}^{1.69}) \times 10^{-5}$. Toward HD 191877 we find $D/H = (0.78 \pm_{0.25}^{0.52}) \times 10^{-5}$ (2σ) and $N/H = (6.76 \pm_{1.57}^{2.22}) \times 10^{-5}$. The O I column density toward HD 191877 is very uncertain. Our preferred value gives $O/H = (3.09 \pm_{0.98}^{1.98}) \times 10^{-4}$, but we cannot rule out O/H values as low as $O/H = 1.86 \times 10^{-4}$, so the O/H value for this sight line should be taken with caution. The D/H ratios along these sight lines are lower than the average value of $(1.52 \pm 0.15) \times 10^{-5}$ (2σ in the mean) found with *FUSE* for the local interstellar medium (~ 37 to 179 pc from the Sun). These observations lend support to earlier detections of variation in D/H over distances greater than a few hundred pc. The O/H ratio toward HD 195965 is supersolar. This star is part of an OB association, so there may be local enrichment by nearby massive stars. The D/H and O/H values measured along these sight lines support the expectation that the ISM is not well mixed on distances of ~ 1000 pc. These observations demonstrate that although D/H studies through Lyman absorption may become impractical at $d > 2500$ pc and $\log N(\text{H I}) > 21$, D/H studies in the distance range from 500 to 2500 pc may be very useful for investigating mixing and chemical evolution in the ISM.

Subject headings: ISM: abundances — ultraviolet: ISM — stars: individual (HD 195965, HD 191877)

1. INTRODUCTION

The abundance of deuterium in the interstellar medium (ISM) is a strong constraint on chemical evolution scenarios. Unlike most elements, the net cosmic abundance of deuterium is not enhanced by stellar processes or supernovae, so its abundance has been declining from the primordial value due to destruction by stellar processing. The primordial abundance of deuterium is itself an important quantity, as it can be used to measure η , the universal ratio of baryons to photons, which can be compared to the predictions of Big Bang nucleosynthesis (Reeves et al. 1973; Boesgaard & Steigman 1985; Burles, Nollett, & Turner 2001).

One approach to finding the initial deuterium abundance is to measure it in high-redshift QSO absorption-line systems, assuming that the clouds which give rise to these systems have undergone very little stellar processing (Webb et al. 1997; Tytler et al. 1999; O’Meara et al. 2001; Pettini & Bowen 2001; Levshakov et al. 2002). However, the large range in D/H values measured in these systems

suggests that the gas in some of these clouds may in fact have undergone some stellar processing (Prantzos & Ishimaru 2001; Fields et al. 2001). It is therefore crucial to understand how chemical evolution affects the abundance of deuterium relative to other elements. Several groups are measuring the abundance of deuterium and other elements along many sight lines in the Galactic ISM in order to establish the mean D/H ratio in the Galactic disk, and to look for variations in the D/H ratio. These variations can shed light on the effects of star-formation history and mixing processes on the D/H ratio. The local D/H value can then be compared to regions that have undergone varying amounts of stellar processing (*e.g.*, high velocity clouds, or intergalactic H I clouds), which will illuminate the effects of stellar processing on the D/H ratio in these systems.

The *Copernicus* satellite was used to measure the D I and H I Lyman series absorption toward ~ 20 stars, and the results suggested a D/H ratio of 1.5×10^{-5} , with a dispersion that may reflect real variations in the ISM (see Vidal-Madjar & Gry 1984 for a review). Several measurements of D/H in the local ISM have been made with the

¹ Department of Physics and Astronomy, Johns Hopkins University, 3400 North Charles Street, Baltimore, MD 21218; choopes@pha.jhu.edu, hwm@pha.jhu.edu, dknauth@pha.jhu.edu

² Space Telescope Science Institute, 3700 San Martin Drive, Baltimore, MD 21218; sembach@stsci.edu

³ Institut d’Astrophysique de Paris, 98 bis Boulevard Arago, 75014 Paris, France; hebrard@iap.fr

Hubble Space Telescope (HST) (Linsky et al. 1995; Linsky & Wood 1996; Linsky 2003; Lemoine et al. 1996; Vidal-Madjar et al. 1998; Hébrard et al. 1999; Sahu et al. 1999; Vennes et al. 2000), though only the Ly α transitions of D I and H I could be analyzed, limiting the number of available sight lines to those with low enough H I columns that the D I absorption is not blended with the H I line but large enough H I columns that D I can be detected. Three sight lines observed with the Interstellar Medium Absorption Profile Spectrograph (*IMAPS*) spanned larger distances than the *HST* sight lines (250 to 500 pc versus $\lesssim 100$ pc), and like the *Copernicus* results they showed evidence of variation in D/H with location (Jenkins et al. 1999; Sonneborn et al. 2000).

One of the science goals of the *Far Ultraviolet Spectroscopic Explorer (FUSE)* is to measure D/H in the Milky Way (Moos et al. 2000). *FUSE* is uniquely suited to do this because it observes the spectral region from 905 to 1187 Å which includes all of the D I Lyman transitions except Ly α . The ability to use multiple D I transitions means that *FUSE* is able to measure $N(\text{D I})$ along higher column density sight lines than missions that only observe Ly α (e.g., *HST*), and for many more sight lines than short term missions (e.g., *IMAPS*). Moos et al. (2002, and references therein) reported results for the first set of seven sight lines ranging from 37 to 179 pc, five of which had both D I measurements (from *FUSE*) and H I (from *HST*). The results were consistent with a single value of $\text{D/H} = (1.52 \pm 0.08) \times 10^{-5}$ (the uncertainty is 1σ in the mean). However, none of these sight lines extend as far as the three sight lines observed by *IMAPS*. Analysis of more extended sight lines is crucial for the verification and understanding of variations in the D/H ratio in the ISM.

In this paper we present *FUSE* measurements of D/H toward two distant stars in the Galactic disk: HD 195965 and HD 191877. These stars are at distances greater than the *IMAPS* targets, extending the distance and range of $N(\text{H I})$ for D/H measurements in the ISM. Information about these two sight lines is listed in Table 1. The *FUSE*, STIS, and ground-based observations and data reduction are described in § 2. Section 3 describes some properties of the sight lines. In § 4 we describe both the curve of growth and the absorption profile fitting analyses of the D I column density toward both stars. In § 5 we discuss the determination of the O I and N I abundances along these sight lines, and in § 6 we re-examine the H I column densities. Section 7 contains a discussion of the results and conclusions.

2. THE DATA

2.1. FUSE Observations

Information for the *FUSE* observations is given in Table 2. The *FUSE* mission and instrument are described by Moos et al. (2000) and Sahnou et al. (2000). The spectra were obtained through the large (30'' \times 30'') LWRS aperture. *FUSE* consists of 4 co-aligned optical channels, two optimized for longer wavelength (LiF1 and LiF2; 1000 – 1187 Å) and two optimized for shorter wavelengths (SiC1 and SiC2; 905 – 1100 Å). All of the deuterium lines used in this paper are located in the SiC channels. The Ly β D I line was not detected in either spectrum because it was blended with the strong H I line, but some lines of

other elements used in our analysis are located in the LiF channels. Between exposures the focal plane assemblies were moved so that the spectra sampled different portions of the detector. This shifting lessens the effects of detector defects when the individual spectra are combined.

The raw spectra were processed through the *FUSE* calibration pipeline (CALFUSE v2.1.6) at the Johns Hopkins University. The pipeline screens data for passage through the South Atlantic Anomaly and low Earth limb angle pointings and corrects for thermal drift of the gratings, thermally-induced changes in the detector read-out circuitry, and Doppler shifts due to the orbital motion of the satellite. Finally, the pipeline subtracts a constant detector background and applies wavelength and flux calibration. After the pipeline reduction the individual spectra were co-added to produce the final calibrated spectrum. The data from the four channels were analyzed separately, because there are slight differences in the spectral resolution between channels, which can cause problems if the channels are co-added. This has the benefit of allowing at least two measurements of each line, a further safeguard against detector defects.

The presence of bright airglow lines at specific regions of the spectrum has resulted in a long-term depletion of electrons in the detector in those regions, and this can cause localized shifts in the spectrum in the dispersion direction. This effect, called “x-walk,” may change the shapes and areas of absorption lines. The effect is more pronounced in certain *FUSE* detectors. We have avoided using the equivalent widths of absorption lines in regions where the x-walk effect is pronounced, so these detector artifacts do not affect the analysis in this paper. The x-walk distortion is described in the *FUSE Observer’s Guide* available at the *FUSE* website (<http://fuse.pha.jhu.edu/>).

Figure 1 shows a portion of the *FUSE* spectrum of HD 195965, and Figure 2 shows the same spectral region for HD 191877. At $\lambda \sim 920$ Å, the shortest wavelengths used in this paper, the signal to noise ratio is $\gtrsim 30:1$ per ~ 20 km s $^{-1}$ resolution element in both spectra, and is considerably higher at longer wavelengths.

2.2. STIS Observations

We observed HD 195965 with the Space Telescope Imaging Spectrograph (STIS) on the *HST* on 2001 October 9 as part of observing program GTO-8487 (P.I.: Moos). Brief information about the observation is given in Table 2. The spectrum was obtained in ACCUM mode using the FUV MAMA, the E140H grating ($\lambda_c = 1307$ Å), and the 0.1'' \times 0.03'' aperture. We reduced the data using CALSTIS (v2.12a) with all of the normal reduction procedures enabled in the standard data pipeline, including the two-dimensional scattered light removal algorithms (see Landsman & Bowers 1997; Lindler & Bowers 2000; see also Howk & Sembach 2000). A description of the STIS pipeline processing steps can be found in the *HST* Data Handbook (Brown et al. 2002).

The extracted STIS spectrum has $S/N \sim 25 - 30$ per spectral resolution element. The spectral resolution of ~ 2.6 km s $^{-1}$ ($R = \lambda/\Delta\lambda \sim 200,000$) is ≈ 11 times better than that available with *FUSE*. The absolute wavelength scale is accurate to 0.5 – 1.0 pixel, or about 3-6 mÅ ($\sim 0.6 - 1.3$ km s $^{-1}$; see Leitherer et al. 2001). The

post-processed STIS data have very low residual backgrounds. We find that the strongly saturated cores of the O I 1302.169 Å and C II 1334.532 Å lines have residual intensities of $\lesssim 1\%$.

2.3. Ground-based Observations

High-resolution echelle spectra of HD 195965 and HD 191877 were taken with the 2.7 m telescope of the University of Texas McDonald Observatory on 2001 December 29. The “2dcoudé” spectrograph (Tull et al. 1995) was used with 1 camera setup and a Tektronix charge-coupled device (CCD) as the detector, which provided high spectral resolution ($R = \lambda/\Delta\lambda \approx 160,000$; $\Delta v \approx 2 \text{ km s}^{-1}$) and covered the wavelength range 6000 Å to 8600 Å. This high resolution mode yielded spectra containing 12 disjoint echelle orders approximately 40 Å wide, separated by approximately 150 Å at 6000 Å. The inter-order separation increased with wavelength until there was approximately 280 Å between orders at near infrared wavelengths. This setup provided spectra on interstellar K I. The resolution was determined from the full width at half maximum (FWHM) of Thorium-Argon (Th-Ar) calibration lamp lines.

The data were reduced in a standard way utilizing the NOAO SUN/IRAF software (v2.11.3). Dark, bias, and flat field lamp exposures were taken to remove any instrumental effects due to the CCD detector. Comparison spectra were taken periodically throughout the night, typically every two hours. The average bias exposure was subtracted from all raw stellar, comparison (Th-Ar) and flat images. The scattered light was fitted by low order polynomials in both the dispersion and spatial directions, and removed. Pixel to pixel sensitivity variations were removed by dividing the normalized average flat field into the stellar spectra. The extracted spectra were placed on a heliocentric wavelength scale using the Th-Ar comparison spectra and corrections for the Earth’s motion. The spectra were co-added and normalized to unity yielding a final spectrum with high signal to noise, approximately 100:1. Figure 3 shows the spectral region near the K I 7698.964 Å line for both sight lines after correcting the velocities to the Local Standard of Rest (for HD 195965 $V_{LSR} = V_{helio} + 16.7 \text{ km s}^{-1}$, and for HD 191877 $V_{LSR} = V_{helio} + 17.4 \text{ km s}^{-1}$).

3. PROPERTIES OF THE SIGHT LINES

HD 195965 ($l=85.71^\circ$, $b=5.00^\circ$) was classified by Morgan, Code, & Whitford (1955) as type B0V. It is listed by Humphreys (1978) as belonging to the Cygnus OB7 association, which is at a distance of $\sim 830 \text{ pc}$ in the Local spiral arm. Diplas & Savage (1994) give a distance of 794 pc from spectroscopic parallax (with an uncertainty of $\sim 25\%$). At this distance it would be 69 pc above the Galactic plane, still well within the thin disk, where most of the cool gas is located. The Hipparcos catalog lists an uncertain distance of the star at $d = 520 \pm_{120}^{230} \text{ pc}$ (ESA 1997). Diplas & Savage (1994) find $\log N(\text{HI})=20.9$ based on *IUE* data.

HD 191877 ($l=61.57^\circ$, $b=-6.45^\circ$) is type B1.0Ib (Morgan et al. 1955), and spectroscopic parallax gives a distance of $\sim 2200 \text{ pc}$ (Diplas & Savage 1994), again with an uncertainty of $\sim 25\%$. This places the star on the edge of the Sagittarius arm and 250 pc below the plane of the

Milky Way, well out of the thin disk (scale height $\sim 100 \text{ pc}$, Dickey & Lockman 1990). It is likely that most of the gas along this sight line lies within $\sim 1000 \text{ pc}$ of the Sun. This is supported by the fact that the H I column toward HD 191877 found by Diplas & Savage (1994) ($\log N(\text{HI})=20.9$) is similar to that toward HD 195965, even though the distance to HD 191877 is more than twice as great as the distance to HD 195965. The two sight lines therefore likely probe a similar distance range in the disk. The Hipparcos distance to HD 191877 is $d > 1160 \text{ pc}$ (ESA 1997).

The ground-based optical spectra of HD 195965 and HD 191877 in Figure 3 reveal that there are multiple clouds along the line of sight to each star. Along both sight lines there appear to be two major components of K I, as well as several weaker components. The STIS spectrum of HD 195965 (Figure 4) confirms the presence of multiple velocity components. Two components are visible in the O I 1355.598 Å profiles, and the S I 1425.030 Å profile shows that the strongest of these is actually two components. The structure in the S I line matches well the K I component structure. The Cl I line shows two additional components at more negative velocities, only one of which is strong enough to appear in the O I 1355.598 Å line. The Cl I line is usually a good tracer of H₂ (Jura 1974), so it appears that the molecular hydrogen velocity structure along the sight line is not complex. The strong O I 1302.168 Å line is completely saturated and shows absorption extending over $\pm 30 \text{ km s}^{-1}$, along with damping wings at even higher velocities.

Both sight lines contain a significant amount of H₂. Most of the unlabeled features in Figures 1 and 2 are H₂ absorption lines. Lines from the lower rotational levels ($J = 0,1,2$) are mostly saturated. These contain most of the H₂ column density, so we did not attempt to determine the H₂ abundance. However, based on the Cl I column toward HD 195965, we estimate roughly $(5 - 10) \times 10^{19} \text{ cm}^{-2}$ on that sight line (Jura 1974). The HD 191877 sight line probably contains a similar amount. There are clearly multiple components along the HD 195965 sight line (revealed by the Cl I line), but they fall within $\pm 15 \text{ km s}^{-1}$, so at *FUSE* resolution the H₂ distribution can be treated as a single component (see § 4.1).

The widths of the K I lines in the spectra of both stars (and the STIS lines in the HD 195965 spectrum) are larger than the resolution of the data. This suggests that there are no strong, narrow (unresolved) features on either sight line. We can use the STIS data for HD 195965 to show this more conclusively for that sight line. Figure 5 shows the apparent column density of S I derived from two different lines: 1295.653 Å and 1296.174 Å. Although the oscillator strengths differ by a factor of ~ 3 (Morton 1991), the derived column density is very similar for the two lines, supporting the conclusion that narrow, saturated features are not present toward HD 195965. (See Savage & Sembach 1991 for a discussion of apparent column density profile comparisons.) In other words, while cold clouds are clearly present, they do not contain a significant amount of the material along these sight lines. Most of the column arises in the diffuse ISM.

To test the effects of the lower resolution of *FUSE* on the analysis of blended lines, we smoothed the absorption

profiles of the S I 1295.653 Å and 1296.174 Å lines in the STIS data by 15 km s⁻¹ to approximate FUSE resolution. We then determined the column densities by summing the apparent optical depth over the line profile. The total column density derived from the 1295.653 Å line is $N(\text{S I}) = (1.21 \pm 0.02) \times 10^{13} \text{ cm}^{-2}$, while that derived from the 1296.174 Å line is $N(\text{S I}) = (1.34 \pm 0.05) \times 10^{13} \text{ cm}^{-2}$. Both values are well within the 1 σ uncertainties of the column densities derived from the unsmoothed profiles, $N(\text{S I}) = (1.26 \pm 0.08) \times 10^{13} \text{ cm}^{-2}$ from the 1295.653 Å line, and $N(\text{S I}) = (1.33 \pm 0.18) \times 10^{13} \text{ cm}^{-2}$ from the 1296.174 Å line. The measured equivalent widths are $17.2 \pm 0.9 \text{ mÅ}$ and $7.4 \pm 1.0 \text{ mÅ}$, similar to the weaker N I and O I lines along the HD 195965 sight line. We also carried out this test on the K I lines shown in Figure 3. Toward HD 191877, the column densities from the unsmoothed profile, $(4.02 \pm 0.06) \times 10^{11} \text{ cm}^{-2}$, agrees well with the column density derived from the smoothed profile, $(3.97 \pm 0.09) \times 10^{11} \text{ cm}^{-2}$. The test was harder to perform on the HD 195965 sight line because of residuals from poorly removed airglow lines, but the column density derived from the unsmoothed profile, $(3.24 \pm 0.16) \times 10^{11} \text{ cm}^{-2}$, is in marginal agreement with that derived from the smoothed profile, $(2.91 \pm 0.19) \times 10^{11} \text{ cm}^{-2}$. With measured equivalent widths of $49.7 \pm 2.1 \text{ mÅ}$ and $62.0 \pm 1.0 \text{ mÅ}$ toward HD 195965 and HD 191877, respectively, these lines are similar in strength to the stronger O I, N I, and D I lines along both sight lines. These tests provide more evidence that there are no unresolved, saturated components along either sight line.

4. THE D I COLUMN DENSITY

The simplest approach to analyzing the chemical composition along a line of sight is to measure the equivalent widths of all lines of a species, assume the material lies in a single component, and construct a Doppler-broadened curve of growth (COG). Since the *FUSE* bandpass contains all of the transitions of D I except for Ly α , in principle this is possible using the current data. In reality, many of the D I transitions are not usable due to interference from neighboring absorption lines. Table 3 lists some of the important interfering lines for the unusable D I transitions along these sight lines. The lower order D I lines are blended with strong H I lines, while higher order lines are often blended with strong H₂ lines. However, in the spectra of each sight line there are four D I transitions that were either free of blending or were blended with weak H₂ lines that could be removed: $\lambda 919.102$, $\lambda 920.713$, $\lambda 922.900$, and $\lambda 925.974$. A more complex but potentially more accurate method is to model the absorption lines with a profile fitting program. This technique can be especially advantageous when the velocity structure of the cloud components is complicated. In this section we describe both of these approaches to determining the D I abundances toward HD 195965 and HD 191877.

4.1. Molecular Hydrogen Removal

There are many H₂ lines in the spectral range around the deuterium lines, and several can potentially affect the measurement of the D I equivalent widths. The lines that affect the four D I lines used in this analysis are listed in Table 4. We include only lines with rotational level $J \leq 5$,

because no higher J level lines were found in the spectra. The lines listed in Table 4 are expected to be strong enough to affect the D I lines. The 920.803 Å line does not fall within the 920.713 Å D I line, but it could affect the continuum on the red side of the line.

To remove the contamination, a line of the same rotational level in a clean part of the spectrum was found to use as a template, following Jenkins et al. (1999). The template line was chosen from the same detector segment as the line being corrected, in order to avoid differences in the line spread function between segments. The parameters of the template lines are listed in Table 4. A Gaussian function was fitted to the template line, and the fit was scaled in optical depth space by the ratio of the $f\lambda$ values to have the strength appropriate for the contaminating line. The template line was chosen to have as close to the same value of $f\lambda$ as the contaminating line as possible in order to avoid saturation effects. The scaled fit was then shifted to the wavelength of the contaminating line and divided out of the observed spectrum around the D I lines. Another H₂ line close in wavelength to the D I line was used to register the position of the scaled line before dividing it out, in order to compensate for any relative errors in the wavelength scale. Figures 6 and 7 show the corrected profiles (solid lines) along with the uncorrected profiles (dashed lines) for both sight lines as a function of LSR velocity.

4.2. Curve of Growth Analysis

Once the H₂ lines were removed, it was necessary to determine the location of the continuum at the position of the D I absorption lines. This was done by fitting low order polynomials across the lines. The situation is complicated by the fact that the D I lines fall on the blue damping wings of the associated H I lines. We used the steeply-sloped blue sides of the H I lines to constrain the fits, and when possible used the red wings of the H I lines as a guide in determining the optimal continuum. Figures 6 and 7 show the absorption profiles of the four D I lines after correction for H₂ for HD 195965 and HD 191877, respectively, along with the adopted continuum placement.

We measured the equivalent widths of the D I lines using the procedures described by Sembach & Savage (1992). The lines were integrated over a velocity range that depended upon the details of the local continuum and line blending. The equivalent widths are listed in Table 5 for HD 195965 and Table 6 for HD 191877. A theoretical single-component COG was fit to the equivalent widths by minimizing χ^2 while varying the column density N and the Doppler parameter b . The final COGs are shown in Figures 8 and 9 for HD 195965 and HD 191877, respectively. The final uncertainties in the equivalent widths were determined from the dispersion of the points about the COG, assuming that a single component COG is appropriate for the sight lines. These error bars are a combination of statistical uncertainties and continuum fitting errors, as described by Sembach & Savage (1992), and include the effects of fixed-pattern noise.

Placing the continuum near the 925.974 Å line was problematic in the spectra of both stars, because of absorption from other elements on the blue side of the absorption line (see Figures 6 and 7). This results in large uncertainties in

the equivalent widths. Because of this the 925.974 Å line is not given as much weight as the other lines in the COG fitting. Table 7 contains the COG D I column density results for both sight lines.

The inset in each COG figure shows a contour plot of the $\Delta\chi^2$ values in the N and b dimensions, with contours of the minimum $\Delta\chi^2+1$, 4, and 9 shown (corresponding to 1, 2, and 3σ). The quoted error bars for N shown in Table 7 are the maximum extent of the projection of the 2σ contour onto the N axis, and likewise for b (listed in the captions to Figures 8 and 9).

4.3. Absorption Profile Fitting

Column densities were also measured independently with the profile fitting procedure Owens.f, following the method described by Hébrard et al. (2002). Briefly, the software simultaneously fits Voigt profiles to all of the unsaturated interstellar lines detected in all *FUSE* segments, using a χ^2 minimization procedure with many free parameters. The free parameters characterize the physical properties of the interstellar clouds (radial velocities, column densities, temperatures, micro-turbulent velocities) as well as the continuum shapes (modeled with polynomials) and possible instrumental effects (line spread function widths, wavelength solution variations). The error bars are obtained using the standard $\Delta\chi^2$ method; they include statistical as well as systematic uncertainties (Hébrard et al. 2002).

The fits include the D I lines 916.6 Å, 919.1 Å, and 920.7 Å, the N I lines 951.1 Å, 951.3 Å, and 959.5 Å, as well as Fe II, and molecular H₂, HD, and CO lines. No O I lines were included in the fits because they are all saturated. Since the H₂ lines were included in the fits, the lines were *not* removed as for the COG analysis (§ 4.1). Samples of the fits are plotted on Figure 10, which presents two spectral windows for each target. The final fits include 30 and 22 spectral windows for HD195965 and HD191877, respectively. The results for $N(\text{D I})$ and $N(\text{N I})$ are reported in Table 7. We obtain $\log N(\text{Fe II}) = 14.81 \pm 0.02$ and 14.95 ± 0.04 (2σ) for HD 195965 and HD 191877, respectively.

5. THE O I AND N I COLUMN DENSITIES

We measured the equivalent widths of O I and N I lines in the *FUSE* spectra using the same techniques as described for D I. The measured equivalent widths are listed in Table 5 for HD 195965 and Table 6 for HD 191877. Figure 11 shows single-component COGs for O I and N I toward HD 195965. The O I lines in the *FUSE* bandpass that are not affected by H₂ absorption do not cover a large range of oscillator strengths, and they mostly fall on the flat part of the COG. The STIS spectrum of HD 195965 adds two O I lines: the 1355.598 Å line on the linear part of the COG, and the 1302.169 Å line, which exhibits damping wings and is on the square root portion of the COG. The STIS lines cover a larger range of oscillator strengths, so the O I abundance toward HD 195965 is well constrained by the *FUSE*+STIS COG. The N I lines in the *FUSE* spectra also cover a large range of oscillator strengths, so an accurate determination of the column density is possible. The derived column densities for O I and N I toward HD 195965 are listed in Table 7.

Figure 12 shows the COGs for O I and N I toward HD 191877. As was the case for HD 195965, the N I abundance is well constrained, but the O I abundance toward HD 191877 is less certain because of the lack of STIS data. A single-component COG fit to the *FUSE* points yields a column density of $\log N(\text{O I}) = 17.24 \pm_{0.22}^{0.42} \text{ cm}^{-2}$ and the Doppler broadening parameter $b = 8.2 \pm_{0.9}^{0.5} \text{ km s}^{-1}$ (2σ). We also set a lower limit of 230 mÅ (3σ) on the 1302.169 Å equivalent width using an *IUE* spectrum of HD 191877 (see § 6). This point rules out the COG found for the *FUSE* points alone, and restricts the O I column density to $\log N(\text{O I}) \geq 17.42 \text{ cm}^{-2}$, with $b = 7.85 \text{ km s}^{-1}$. The b -values derived from the COGs for N I and O I toward HD 195965 are almost identical, suggesting that the velocity behavior of these two species is coupled. If we assume that this is also true for the HD 191877 sight line and force $b = 7.5 \text{ km s}^{-1}$ for the O I COG (the solid line in the top panel of Figure 12), the derived column density of O I is $\log N(\text{O I}) = 17.54 \pm_{0.12}^{0.20} \text{ cm}^{-2}$ (2σ). Although the HD 195965 sight line suggests that O I and N I are coupled, we cannot know with certainty whether this is also true along the HD 191877 sight line. This exercise illustrates the fact that the O I column density toward HD 191877 is not well constrained by the lines in the *FUSE* spectrum. We adopt the larger $N(\text{O I})$ column density as our preferred value, but note that it should be treated with caution.

We also used the damping wings of the O I 1302.169 Å line in the STIS spectrum of HD 195965 to make an independent determination of the O I abundance toward the star. We fit a single component Voigt profile to the normalized O I line using an oscillator strength $f = 0.04887$ and a natural damping constant $\gamma = 5.75 \times 10^8 \text{ s}^{-1}$ (Morton 1991). The best fit model has a central velocity $v_{\text{helio}} = +2.1 \text{ km s}^{-1}$, $b = 6.3 \pm 0.3 \text{ km s}^{-1}$, and $\log N(\text{O I}) = 17.80 \pm_{0.09}^{0.05} \text{ cm}^{-2}$ (2σ). This column density is in excellent agreement with the COG result listed in Table 7. The single-component fit to the O I 1302.169 Å line is shown in Figure 13. The fit shown in the figure reproduces the observed absorption profile core and damping wings well, with the minor exception of a slight underestimate in the absorption strength between +21 and +40 km s^{-1} . This additional absorption is likely due to very low column density gas along the sight line that does not contribute much to the total column density; a component with an O I column density of $\sim 10^{13} \text{ cm}^{-2}$ could account for this minor discrepancy. Experimentation with additional components does not change the best-fit result substantially. Performing a fit with the O I column density divided among two components separated by $\sim 12 \text{ km s}^{-1}$ as suggested by the O I 1355.598 Å line shown in Figure 4 yields a best fit nearly indistinguishable from the single-component fit shown in Figure 13.

The O I 1302.169 Å line is very strong, and can be used to test for the presence of high-velocity components that might contribute to the column density of H I but be outside of velocity integration range for other elements. The most obvious candidate is the component between +21 and +40 km s^{-1} , which contributes only $N(\text{O I}) \sim 10^{13} \text{ cm}^{-2}$, corresponding to $N(\text{H I}) \sim 3 \times 10^{16} \text{ cm}^{-2}$ using the O/H ratio of 3.43×10^{-4} from Meyer (2001), or $\sim 3 \times 10^{-5}$ of the total H I column density (see § 6). No other compo-

nents this strong are visible in Figure 13, so we conclude that high-velocity H I is not an issue for the HD 195965 sight line.

The STIS spectrum of HD 195965 contains both the optically thin 1355.598 Å line and the damped 1302.169 Å line. We can use this fact to test for consistency between the oscillator strengths of the two lines (see Sofia, Cardelli, & Savage 1994). The O I column densities derived from these lines are $N(\text{O I}) = (5.7 \pm 1.1) \times 10^{17} \text{ cm}^{-2}$ and $(6.3 \pm 0.5) \times 10^{17} \text{ cm}^{-2}$, respectively (uncertainties are 1σ). These results are identical within the uncertainty, which suggests that any error the oscillator strength of either line is less than 20% (the uncertainty in the 1355.598 Å equivalent width). The oscillator strength for the 1355.598 Å line listed in Table 5 includes the correction from Welty et al. (1999).

6. THE H I COLUMN DENSITY

We have re-measured the H I column densities for the HD 191877 and HD 195965 sight lines using existing STIS and *IUE* data. Single-component Voigt profiles were fit to the H I absorption toward each star. The fits were limited to the 1170 to 1260 Å spectral region, with the overall continuum levels determined at longer wavelengths, as needed. For both sight lines, the fit is insensitive to the assumption of a single absorbing component. Adding additional components or changing the b -value of the absorption (assumed to be in the 1 to 100 km s^{-1} range) did not alter the fits significantly since the quality of the fits is governed primarily by the steep walls of the line cores and the broad radiation-damping wings. The Voigt profile fitting method has been described in detail for H I determinations in previous *FUSE* D/H papers (see Moos et al. 2002, and references therein). Our analyses follow many of these same principles and methods.

For HD 195965, we used the STIS E140H data available in this wavelength region (see §2.2) to determine the H I column density. We paid special attention to making sure that the flux calibration mapping at the ends of the individual echelle orders was consistent between adjoining orders. Scattered light is not a significant source of uncertainty in the final measurement since we used the damping wings of the lines rather than the saturated portion of the line core to determine the H I column density. We find a best-fit value of $\log N(\text{H I}) = 20.95 \pm 0.05$ (2σ) for the fit to the high quality STIS data shown in Figure 14. This value is slightly higher than, but within the errors of, the former value of 20.90 ± 0.09 (1σ) found by Diplas & Savage (1994) using the "continuum reconstruction" technique on existing *IUE* data. The reconstruction method and profile fitting methods are complimentary to each other. The fit is shown in the bottom panel of Figure 14, together with the fits appropriate for the $\pm 2\sigma$ column density ranges (dashed lines). For this sight line, the higher quality STIS data more tightly defines the extent of the H I absorption than the *IUE* data, and as can be seen in the top panel of Figure 14, the resulting fit is consistent with the *IUE* small aperture data analyzed previously.

The primary difficulty in fitting the STIS profile of HD 195965 arises in the wavelength region between 1222 and 1225 Å, where the fit slightly overestimates the amount of absorption present. We explored other mod-

els that fit this region better (at the expense of fit quality at other wavelengths) and found that in all cases the resulting column density was within the listed uncertainties. Therefore, while we are uncertain of the exact cause of the discrepancy in this wavelength region, we believe the resulting H I column density is a robust estimate. Note that this portion of the STIS spectrum contains the border between two echelle orders, and that the anomaly is not apparent in the *IUE* spectrum.

For HD 191877, we re-examined the *IUE* small aperture data (SWP02837) available for this sight line. A more recent exposure (SWP148425) taken through the small aperture clearly has problems with the flux levels as a result of poor centering; we did not use this low quality spectrum. We find $\log N(\text{H I}) = 21.05 \pm 0.10$ (2σ), which again is slightly larger than, but consistent with, the previous estimate of 20.90 ± 0.10 (1σ) found by Diplas & Savage (1994). The fit is shown in Figure 15, along with the $\pm 2\sigma$ error bars. As can be seen from this figure, a fit with a smaller column, like the one preferred by the previous investigators, is clearly below the true column density (see the -2σ [$\log N = 20.95$] model in the figure). Diplas & Savage note that there may be a small amount (~ 0.01 dex) of contamination by stellar absorption in the H I Ly α profile. This contamination does not affect our $N(\text{H I})$ estimate significantly.

7. DISCUSSION

The sight lines analyzed in this paper are the longest ones for which the D I column densities have been determined with *FUSE*. As such, they present the opportunity to look for variations in D I/H I, D I/O I, and D I/N I beyond the local ISM sight lines presented by Moos et al. (2002). Table 8 contains column density ratios of various elements toward both stars, along with the mean values for the local ISM from Moos et al. (2002). In this section we discuss the behavior of these column density ratios beyond the local ISM.

7.1. D/H

The deuterium abundances along seven sight lines have been analyzed with *FUSE* (Moos et al. 2002; Kruk et al. 2002; Friedman et al. 2002; Sonneborn et al. 2002; Lemoine et al. 2002; Lehner et al. 2002; Wood et al. 2002; Hébrard et al. 2002). Five of these had both D I and H I measurements, and the results were consistent with a constant value of D/H in the local ISM. Earlier *Copernicus* observations showed evidence for variations in D/H at larger distances (see Vidal-Madjar & Gry 1984 for a review), evidence which was strengthened by subsequent *IMAPS* investigations (Jenkins et al. 1999; Sonneborn et al. 2000). The main obstacle to verifying and understanding this variation is the paucity of suitable deuterium sight lines that probe distances ≥ 250 pc.

Figure 16 shows the D/H ratios for HD 195965 and HD 191877 plotted as a function of distance from the Sun, along with five of the seven original *FUSE* sight lines with reliable H I measurements, and several others from *HST*, *IMAPS*, and *Copernicus* (see Moos et al. 2002). The D/H ratios toward both stars are lower than the average value found for the original seven *FUSE* sight lines. This contrasts with the lack of variation seen in the local ISM. The

new sight lines support the existence of variations in the D/H ratio at distances larger than a few hundred pc, as also suggested by *IMAPS* and *Copernicus*.

In the simplest model of chemical evolution, stellar processing (astration) leads to a decline in the D/H ratio because D is easily destroyed in stars. Thus, the D/H ratio is expected to vary among regions of the Galaxy that have undergone different amounts of star formation in the past, provided that the gas in these regions has not mixed (*e.g.* Tosi et al. 1998; Chiappini et al. 2002). In a small volume like the local ISM ($r = 100$ pc), Moos et al. (2002) showed that the time between supernova t_{SN} is roughly equal to the mixing time scale (assumed to be the sound crossing time t_s), suggesting that the gas in such a region is well-mixed. If a larger region is considered, say 1000 pc in radius to approximate the scales probed by HD 195965 and HD 191877, the crossing time increases by a factor of 10, while the time between supernovae decreases by a factor of 100, so that $t_{SN} \ll t_s$. Supernovae are not distributed randomly over this region but are spatially correlated in regions of star formation, meaning that substantial inhomogeneities will arise between star-forming regions and more quiescent regions. For these reasons it is not surprising to see variations over the distances probed by HD 195965 and HD 191877.

A more precise treatment of mixing in the ISM was carried out by de Avillez & Mac Low (2002). Using numerical simulations, they found that the mixing time scales were a few times 10^8 years. Chemical inhomogeneities in the ISM are long-lived, so variations in D/H are expected over 1000 pc length scales. In fact, since the mixing time scales increase only slightly with length scale in their models, it is unlikely that the local ISM (*e.g.*, the original seven *FUSE* sight lines) would have a constant D/H value if any sources of inhomogeneities (*i.e.*, supernovae) have occurred within the past $\sim 10^8$ years.

We have investigated several alternative explanations for the low D/H values. One possibility is that some of the D column is in high-velocity components which are outside of the velocity integration range used to determine $N(\text{D I})$ (Jenkins et al. 1999). We have used the O I 1302.169 Å line in the STIS spectrum of HD 195965 to rule this out for that sight line (see § 5). Note that $\sim 50\%$ of the D I column would have to be missed if the D/H ratio for the HD 191877 sight line were as high as the Moos et al. (2002) mean local ISM value. Figure 7 shows that this is not the case, although we cannot rule out a much smaller systematic offset for HD 191877.

A second possibility is that a significant amount of D is locked up in HD molecules. To test this idea, we have measured the equivalent widths of several strong, isolated Lyman series HD lines in the *FUSE* spectra: (3-0) R(0) 1066.271 Å, (5-0) R(0) 1042.847 Å, and (4-0) R(0) 1054.288 Å. The column densities derived from the equivalent widths are $\sim 2.4 \times 10^{14} \text{ cm}^{-2}$ for the HD 195965 sight line, and $\sim 3.0 \times 10^{14} \text{ cm}^{-2}$ for the HD 191877 sight line. For both sight lines this is $\lesssim 3.5\%$ of the total D column density, much lower than the uncertainty in $N(\text{D I})$.

7.2. O/H

The D/O and O/H ratios toward HD 195965 in Table 8 are quite different from the average values in the local ISM

found by Moos et al. (2002). This is a surprising result, since Meyer et al. (1998) found very little variation in O/H in their survey, which covered distances and H I column densities similar to those of the sight lines in this paper. Both the O I and H I column densities toward HD 195965 were determined through at least two independent methods, with very similar results. The H I was measured using both *IUE* and STIS data, and the O I was measured with a single-component COG which combined *FUSE* and STIS data, as well as independent estimates from the optically thin 1355.598 Å line and the damped 1302.169 Å line in the STIS spectrum. Both of these column densities are therefore quite firmly established, and we believe that it is very unlikely that there is a substantial systematic error in either quantity.

HD 195965 appears to lie on a very high metallicity sight line, with supersolar O/H (Sofia & Meyer 2001). This may be a region where the signature of stellar processed gas is still visible (as is not the case for the local bubble). Humphreys (1978) found that this star is in the Cygnus OB7 association. If so, it may be in a peculiar region, perhaps in a metal-enriched cloud of ejecta from the star itself or a neighbor. Since gas with high metallicity is thought to have undergone stellar processing, D/H in such gas is expected to be low. This expected anticorrelation between O/H (or N/H) and D/H was not seen in the first seven *FUSE* sight lines, although it could have been masked by the small number of sight lines studied (Steigman 2002). Figure 17 compares the O/H and D/H value for HD 195965 with those of the original seven *FUSE* sight lines. Unfortunately HD 195965 is the only point at high metallicity, so no firm conclusions can be drawn. However, it is possible that this sight line shows evidence of the expected anticorrelation in the ISM (see also Steigman 2002). Note that an error in the H I column density toward HD 195965 would tend to move that point along a diagonal line with a positive slope, and thus could not produce the expected trend of decreasing D/H with rising O/H.

The HD 191877 sight line lacks STIS data, so we could not constrain the O I and H I abundances with multiple estimates. For these reasons we are less confident in the O I column densities found for the HD 191877 sight line. As discussed in § 5, the derived $\log N(\text{O I})$ is very uncertain, although our preferred value, found by coupling the b -values of N I and O I, is consistent with the *FUSE* local ISM ratio and the Meyer et al. (1998) ratio. Unfortunately, with the existing information, we cannot make any strong conclusions about O/H toward HD 191877.

7.3. N/H

The N/H ratios toward HD 195965 and HD 191877 in Table 8 are higher than the average values in the local ISM found by Moos et al. (2002). Figure 18 shows a plot of N/H versus D/H along both sight lines, compared to the four *FUSE* sight lines for which N/H was measured. The figure is very suggestive of an anticorrelation between D/H and N/H.

Complicating the interpretation of this plot is the fact N/H ratio is susceptible to ionization effects, especially at low column densities which do not provide adequate shielding from ionizing photons, such as the column densities along the local ISM sight lines (Jenkins et al. 2000).

The dashed line in Figure 18 shows the ISM value of N/H found by Meyer et al. (1997). The sight lines used in that study had higher H I column densities than the *FUSE* local ISM sight lines, so the *FUSE* sight lines are very likely underestimating N/H, because a significant fraction of N is ionized. The apparent trend in Figure 18 may simply reflect the tendency for $N(\text{N II})/N(\text{N I})$ to decrease with increasing $N(\text{H I})$.

However, an anticorrelation between D and N abundances would be expected if D is destroyed in stars while N is produced (*e.g.* Steigman et al. 2002). The overabundance of heavy elements accompanied by the underabundance of D seems to fit well within a simple chemical evolution scenario. While ionization effects probably play a role in the high N/H ratio on these sight lines, they may not be the only factor. A comprehensive N/H survey using *FUSE* spectra is currently underway, and may shed light on this issue.

Several sight lines do not follow the expected trend of low D/H accompanied by high N/H or O/H. Sonneborn et al. (2002) found a low O/H ratio toward BD+28°4211 with *FUSE*, while their D/H ratio is close to the Local ISM mean. Jenkins et al. (2000) found a low D/H toward δ Orionis using *IMAPS*, but also a somewhat low N/H ratio. These deviations suggest that the simple picture of increasing heavy elements abundances with decreasing D/H is not complete.

7.4. Future Prospects for D/H Measurements

Measuring D/H values in the Milky Way becomes increasingly difficult as $N(\text{H I})$ increases, perhaps reaching a fundamental confusion limit. The COGs in Figures 8 and 9 show that the high order D I Lyman transitions are close to saturation. At higher column densities, these transitions will fall on the flat part of the COG and will not give precise column density information. Even higher order transitions at shorter wavelengths, where the D I lines might not yet be saturated at higher column density, are not useful because the H I transitions begin to blend together. These facts make it unlikely that many

Galactic disk sight lines more distant than those studied here will be useful for D/H measurements. However, the sight lines analyzed in this paper demonstrate that D/H properties over the distance range from 500 to 2500 pc can be explored with *FUSE*, even if these sight lines contain a significant amount of H₂. This first glimpse at D/H in this distance range suggests that it will be very useful for understanding mixing and chemical evolution in the ISM.

The chemical evolution model of Chiappini et al. (2002) predicts an increase in D/H with galactocentric radius, accompanied by a decrease in N/H and O/H, leading to a pronounced gradient in D/O and N/O. The gas in the outer parts of the galaxy has undergone less stellar processing, and in fact Chiappini et al. (2002) predict that the D/H ratios in the outer disk will approach the primordial value. The sight lines studied here have roughly the same galactocentric radii as the local ISM sight lines of Moos et al. (2002), so we cannot test this model, but with *FUSE* observations of sight lines in the inner and outer Galactic disk this may prove possible.

We would like to thank Ed Jenkins, Gary Steigman, Jeffrey Linsky, Cristina Oliveira, and Paule Sonnentrucker for enlightening discussions. This work is based on data obtained for the Guaranteed Time Team by the NASA-CNES-CSA *FUSE* mission operated by the Johns Hopkins University. Financial support to U. S. participants has been provided by NASA contract NAS5-32985. French participants are supported by CNES. This work was partly supported by NASA Guaranteed Time Observer funding to the STIS Science Team under NASA contract NAS5-30403 and is based upon observations obtained with the NASA/ESA Hubble Space Telescope, which is operated by the Association of Universities for Research in Astronomy, Inc., under NASA contract NAS5-26555. This work has made use of the profile fitting procedure Owens.f developed by M. Lemoine and the FUSE French Team. GH would like to thank Sylvestre Lacour and Arielle Moullet. DK thanks the staff at McDonald Observatory, especially David Doss.

REFERENCES

- Abgrall, H., Roueff, E., & Drira, I. 2000, *A&AS*, 141, 297
 de Avillez, M. A. & Mac Low, M.-M. 2002, *ApJ*, in press [astro-ph/0209441]
 Boesgaard, A. M. & Steigman, G. 1985, *ARA&A*, 23, 319
 Brown, T., et al. 2002, in *The HST Data Handbook* (v4.0), ed. B. Mobasher, (Baltimore: STScI)
 Burles, S., Nollett, K. M., & Turner, M. S. 2001, *ApJ*, 552, L1
 Chiappini, C., Renda, A., & Matteucci, F. (2002), *A&A*, in press [astro-ph/0209240]
 Dickey, J. M. & Lockman, F. J. 1990, *ARA&A*, 28, 215
 Diplas, A. & Savage, B. D. 1994, *ApJS*, 93, 211
 ESA, 1997, *The Hipparcos and Tycho Catalogues*, ESA SP-1200
 Fields, B. D., Olive, K. A., Silk, J., Cassé, M., & Vangioni-Flam, E. 2001, *ApJ*, 563, 653
 Friedman, S. D., et al. 2002, *ApJS*, 140, 37
 Hébrard, G., et al. 2002, *ApJS*, 140, 103
 Hébrard, G., Mallouris, C., Ferlet, R., Koester, D., Lemoine, M., Vidal-Madjar, A., & York, D. 1999, *A&A*, 350, 643.
 Howk, J. C. & Sembach, K. R. 2000, *AJ*, 119, 2481.
 Humphreys, R. M. 1978, *ApJS*, 38, 309
 Jenkins, E. B., Tripp, T. M., Woźniak, P. R., Sofia, U. J., & Sonneborn, G. 1999, *ApJ*, 520, 182.
 Jenkins, E. B. et al., 2000, *ApJ*, 538, L81
 Jura, M. 1974, *ApJ*, 190, L33
 Kruk, J. W., et al. 2002, *ApJS*, 140, 19
 Landsman, W., & Bowers, C. 1997, in *HST Calibration Workshop with a New Generation of Instruments*, eds. S. Casertano, R. Jedrzejewski, C.D. Keyes, & M. Stevens (Baltimore: STScI), 132
 Landsman, W. B., Henry, R. C., Moos, H. W., & Linsky, J. L. 1984, *ApJ*, 285, 801.
 Lehner, N., Gry, C., Sembach, K. R., Hébrard, G., Chayer, P., Moos, H. W., Howk, J. C., & Désert, J.-M. 2002, *ApJS*, 140, 81
 Leitherer, C., et al. 2001, *STIS Instrument Handbook* (v5.1), (Baltimore: STScI)
 Lemoine, M., Vidal-Madjar, A., Bertin, P., Ferlet, R., Gry, C., & Lallement, R. 1996, *A&A*, 308, 601
 Lemoine, M., et al. 2002, *ApJS*, 140, 67
 Levshakov, S. A., Dessauges-Zavadsky, M., D’Odorico, S., & Molaro, P. 2002, *ApJ*, 565, 696.
 Lindler, D., & Bowers, C. 2000, *BAAS*, 197, 12.02
 Linsky, J. L., 2002 *Space Science Reviews*, in press
 Linsky, J. L., Diplas, A., Wood, B. E., Brown, A., Ayres, T. R., & Savage, B. D. 1995, *ApJ*, 451, 335
 Linsky, J. L. & Wood, B. E. 1996, *ApJ*, 463, 254.
 Meyer, D. M. 2001, *XVIIth IAP Colloq. Gaseous Matter in Galaxies and Intergalactic Space*, ed. R. Ferlet & M. Lemoine, (Paris: Editions Frontières)
 Meyer, D. M., Cardelli, J. A., & Sofia, U. J. 1997, *ApJ*, 490, L103
 Meyer, D. M., Jura, M., & Cardelli, J. A. 1998, *ApJ*, 493, 222
 Moos, H. W. et al. 2000, *ApJ*, 538, L1

- Moos, H. W., Sembach, K. R., Vidal-Madjar, A., York, D. G., et al. 2002, *ApJS*, 140, 3
- Morgan, W. W., Code, A. D. & Whitford, A. E. 1955, *ApJS*, 2, 41
- Morton, D. C. 1991, *ApJS*, 77, 119
- O'Meara, J. M., Tytler, D., Kirkman, D., Suzuki, N., Prochaska, J. X., Lubin, D., & Wolfe, A. M. 2001, *ApJ*, 552, 718.
- Pettini, M. & Bowen, D. V. 2001, *ApJ*, 560, 41.
- Prantzos, N. & Ishimaru, Y. 2001, *A&A*, 376, 751.
- Reeves, H., Audouze, J., Fowler, W. A., & Schramm, D. N. 1973, *ApJ*, 179, 909.
- Sahnow, D. J. et al. 2000, *ApJ*, 538, L7
- Sahu, M. S. et al. 1999, *ApJ*, 523, L159.
- Sembach, K. R. & Savage, B. D. 1992, *ApJS*, 83, 147.
- Sofia, U. J., Cardelli, J. A., & Savage, B. D. 1994, *ApJ*, 430, 650
- Sofia, U. J. & Meyer, D. M. 2001, *ApJ*, 554, L221
- Sonneborn, G., et al. 2002, *ApJS*, 140, 51
- Sonneborn, G., Tripp, T. M., Ferlet, R., Jenkins, E. B., Sofia, U. J., Vidal-Madjar, A., & Woźniak, P. R. 2000, *ApJ*, 545, 277.
- Steigman, G. 2002, *ApJ*, in press [astro-ph/0209246]
- Tull, R. G., MacQueen, P. J., Sneden, C., & Lambert, D. L. 1995, *PASP*, 107, 251
- Tytler, D., Burles, S., Lu, L., Fan, X., Wolfe, A., & Savage, B. D. 1999, *AJ*, 117, 63.
- Vennes, S. L., Polomski, E. F., Lanz, T., Thorstensen, J. R., Chayer, P., & Gull, T. R. 2000, *ApJ*, 544, 423.
- Vidal-Madjar, A. & Gry, C. 1984, *A&A*, 138, 285.
- Vidal-Madjar, A. et al., 1998, *A&A*, 338, 694
- Webb, J. K., Carswell, R. F., Lanzetta, K. M., Ferlet, R., Lemoine, M., Vidal-Madjar, A., & Bowen, D. V. 1997, *Nature*, 388, 250
- Welty, D. E., Hobbs, L. M., Lauroesch, J. T., Morton, D. C., Spitzer, L., & York, D. G. 1999, *ApJS*, 124, 465
- Wood, B. E., Linsky, J. L., Hébrard, G., Vidal-Madjar, A., Lemoine, M., Moos, H. W., Sembach, K. R., & Jenkins, E. B. 2002, *ApJS*, 140, 91
- York, D. G. & Rogerson, J. B. 1976, *ApJ*, 203, 378.

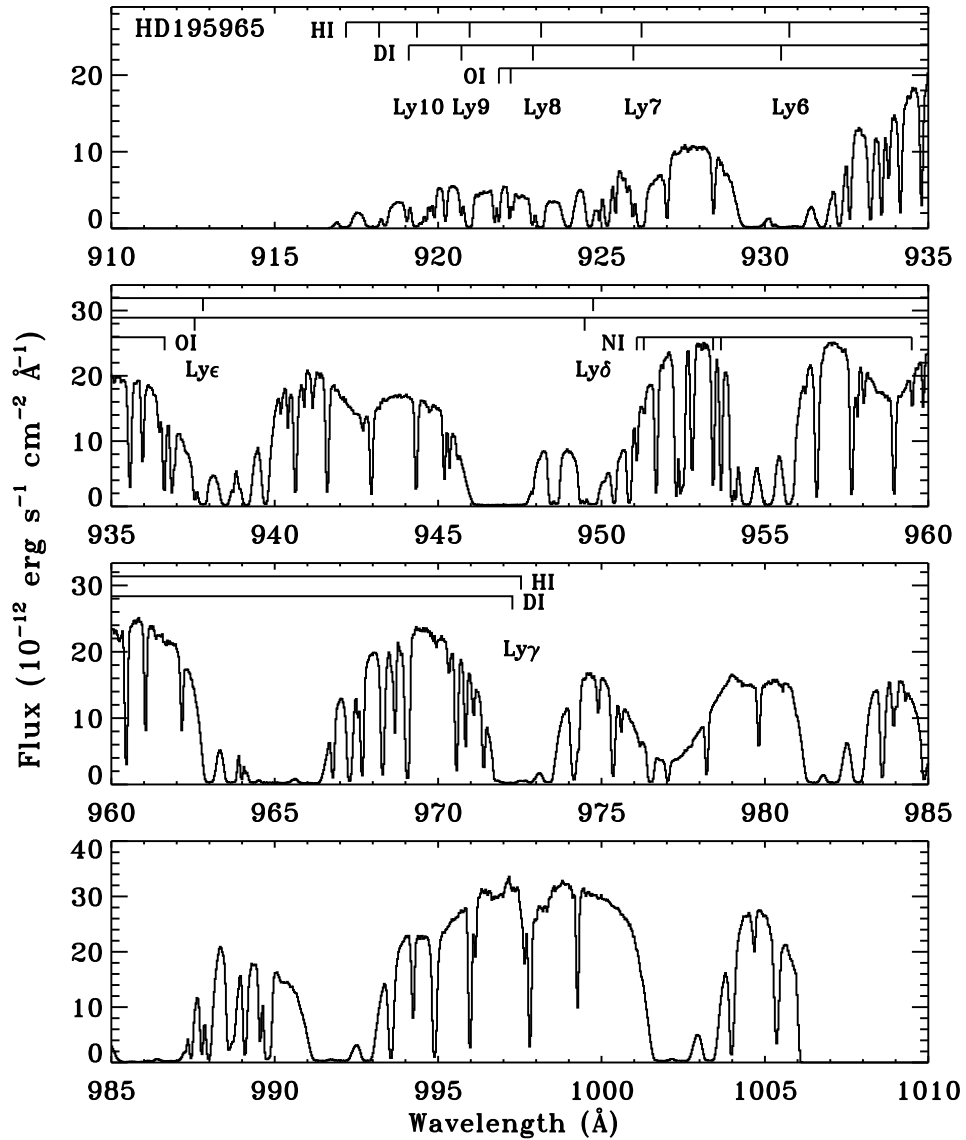


FIG. 1.— A portion of the *FUSE* SiC2 spectrum of HD 195965. The Lyman transitions of H I and D I are labeled, as are the O I and N I transitions in this region of the spectrum that were used in the analysis. The D I transitions used in the curves of growth were Ly7, Ly8, Ly9, and Ly10. Most of the other features are H₂ absorption lines. The spectrum shown here is binned by 5 pixels to ~ 10 km s $^{-1}$ bins for display.

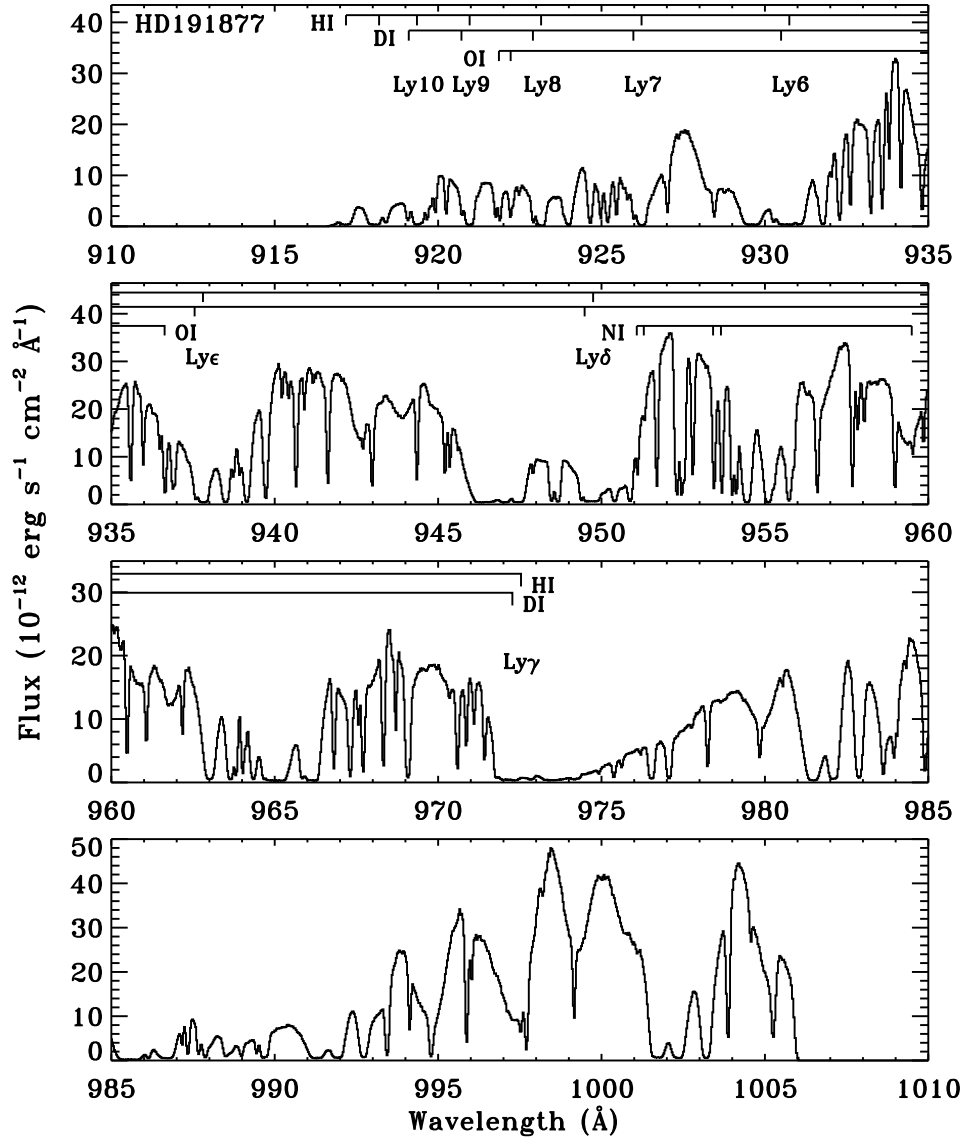


FIG. 2.— A portion of the *FUSE* SiC2 spectrum of HD 191877. The Lyman transitions of H I and D I are labeled, as are the O I and N I transitions in this region of the spectrum that were used in the analysis. The D I transitions used in the curves of growth were Ly7, Ly8, Ly9, and Ly10. Most of the other features are H₂ absorption lines. The spectrum shown here is binned by 5 pixels to ~ 10 km s^{-1} bins for display.

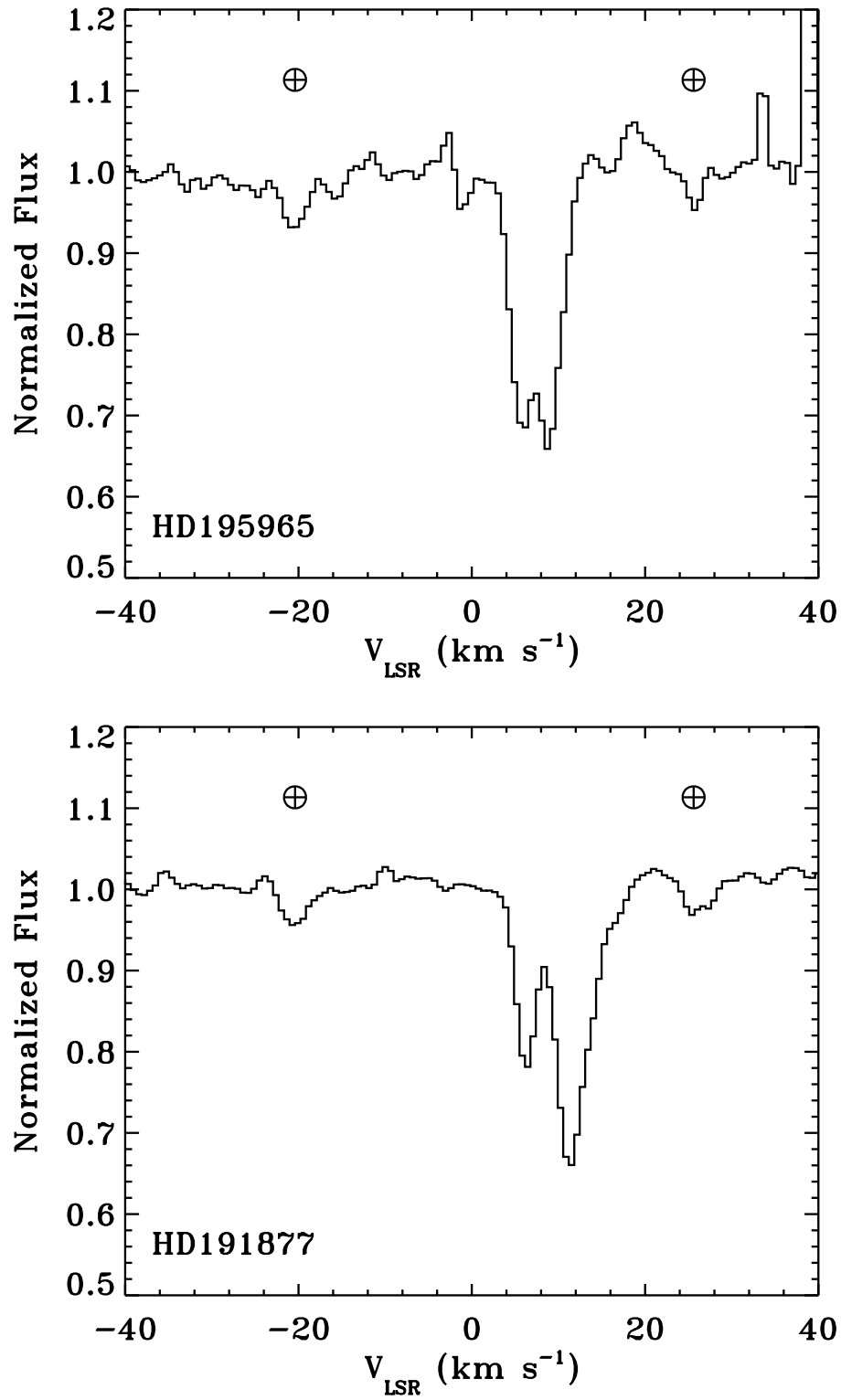


FIG. 3.— Absorption profiles of the K I 7698.964 Å line for both stars. The absorption lines at -20 km s^{-1} and $+28 \text{ km s}^{-1}$ are remnants of atmospheric H₂O lines.

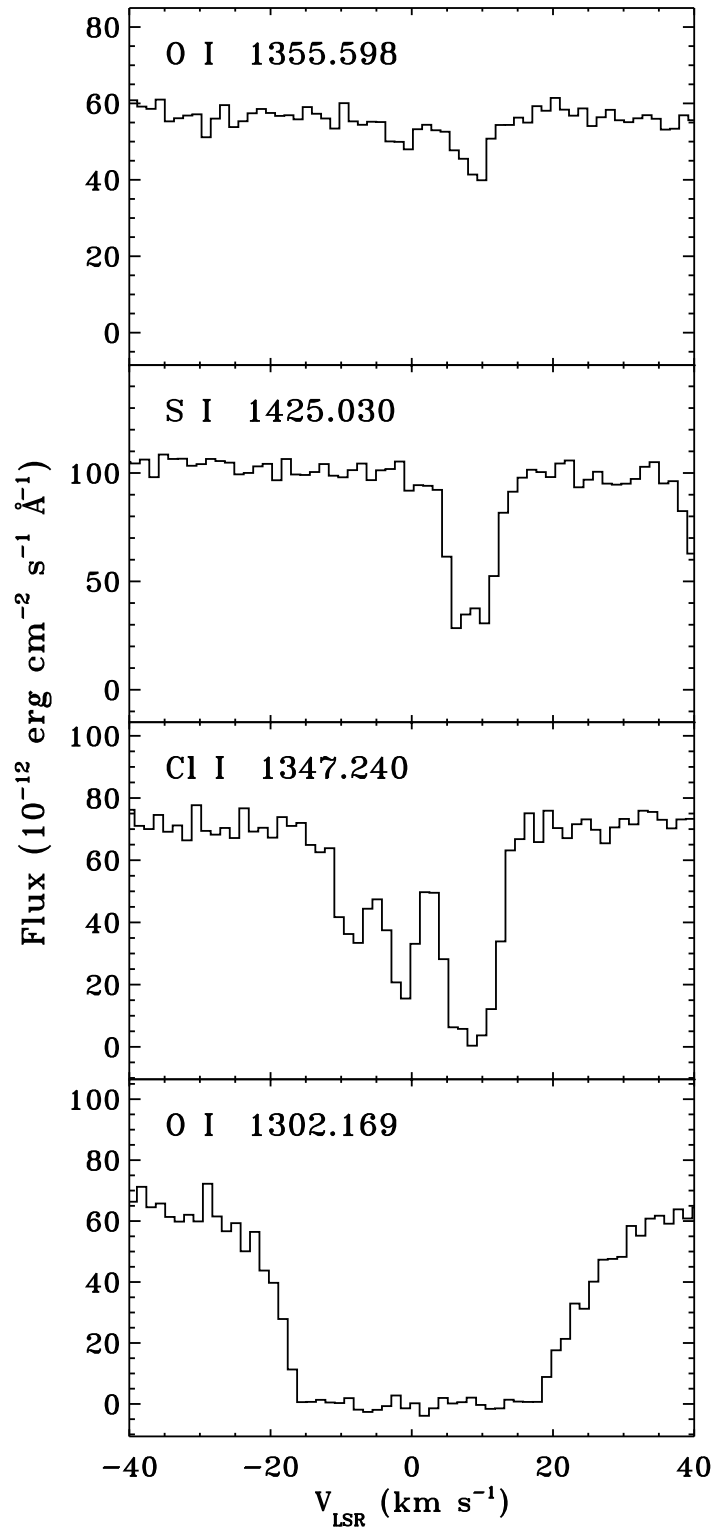


FIG. 4.— Absorption profiles of selected lines from the STIS spectrum of HD 195965.

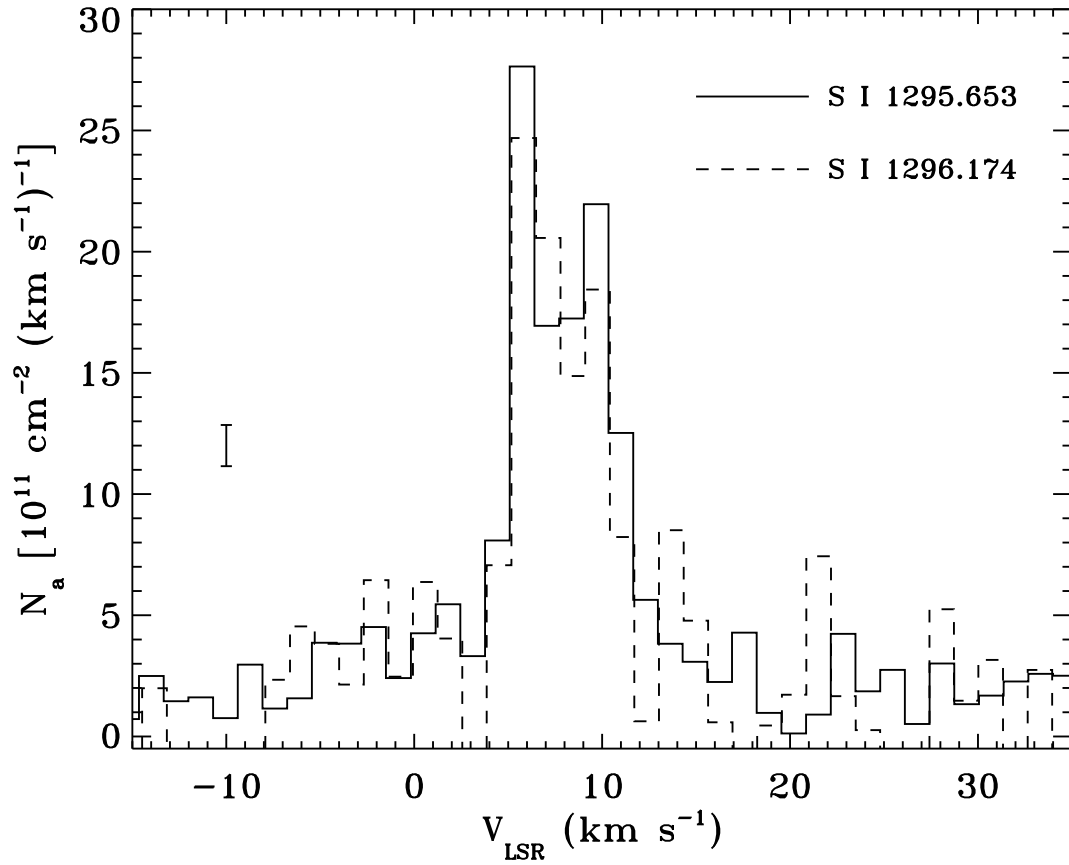


FIG. 5.— Comparison of the apparent column density profiles derived from two S I lines in the STIS spectrum of HD 195965. The strengths ($f\lambda$) of the two lines differ by a factor ~ 3 , but the apparent column densities are similar at all velocities. The total column density between 3 and 13 km s^{-1} derived from the 1295.653 \AA line is $N(\text{S I}) = (1.26 \pm 0.08) \times 10^{13} \text{ cm}^{-2}$, while that derived from the 1296.174 \AA line is $N(\text{S I}) = (1.33 \pm 0.18) \times 10^{13} \text{ cm}^{-2}$. A representative error bar is shown.

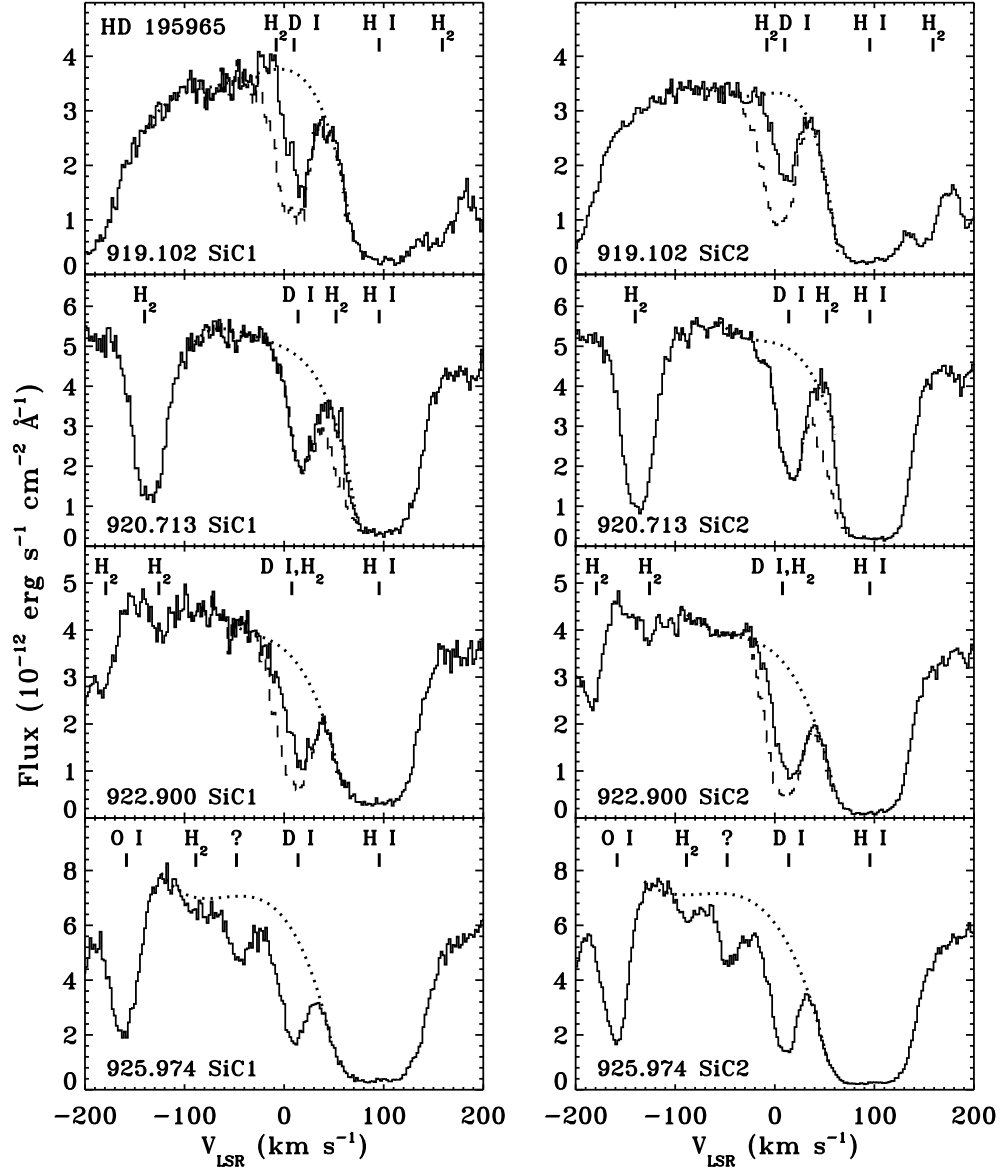


FIG. 6.— Four D I absorption profiles in the *FUSE* HD 195965 spectra. The 919.102 Å, 920.713 Å, and 922.900 Å profiles have been corrected for H₂ absorption. The uncorrected profiles are also shown (dashed lines). The 925.974 Å profile is not affected by H₂ absorption. The adopted continua are shown as dotted lines. The feature at 925.780 Å (−45 km s^{−1} in the bottom panels) is unidentified.

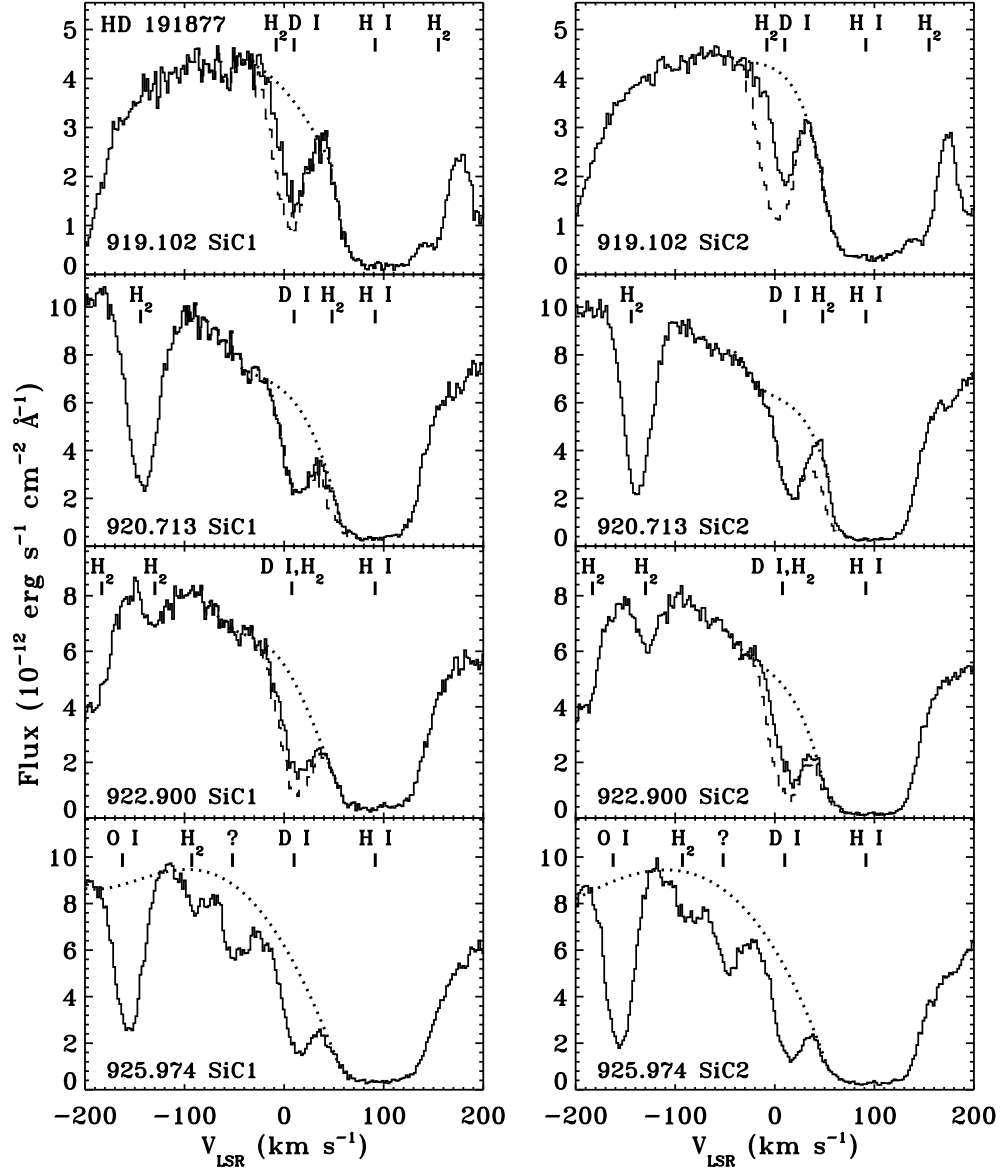


FIG. 7.— Four D I absorption profiles in the *FUSE* HD 191877 spectra. The 919.102 Å, 920.713 Å, and 922.900 Å profiles have been corrected for H₂ absorption. The uncorrected profiles are also shown (dashed lines). The 925.974 Å profile is not affected by H₂ absorption. The adopted continua are shown as dotted lines. The feature at 925.780 Å (−45 km s^{−1} in the bottom panels) is unidentified.

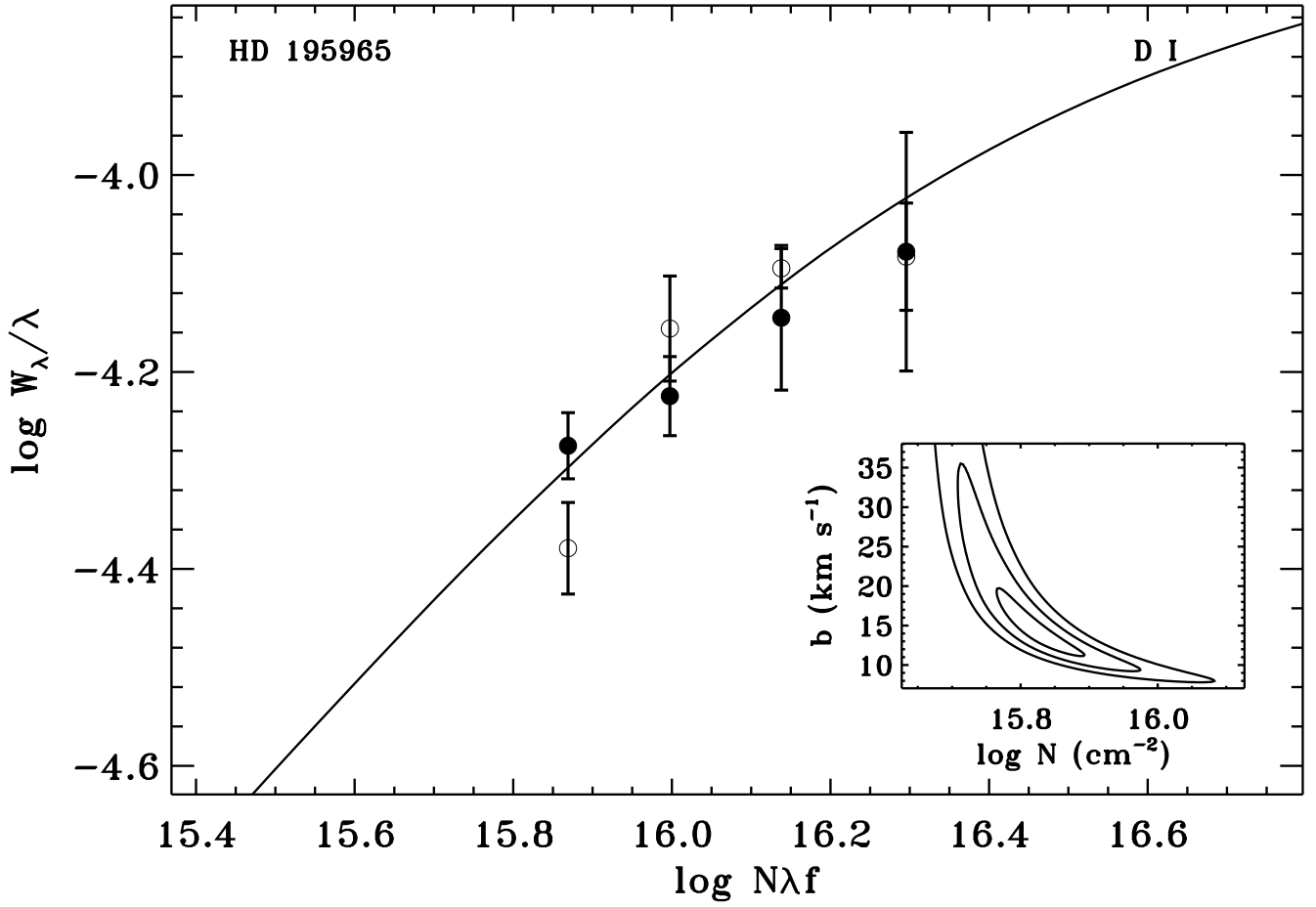


FIG. 8.— The best fit single-component curve of growth for D I toward HD 195965, which gives $\log N(\text{D I})=15.83 \pm_{0.11}^{0.14}$ (2σ) and $b = 14.1 \pm_{4.7}^{21.4}$ km s^{-1} (2σ). The filled circles are points measured from the SiC1 channel, and the open circles are points measured from the SiC2 channel. The inset shows a contour plot of the χ^2 distribution, with the 1σ , 2σ , and 3σ contours shown.

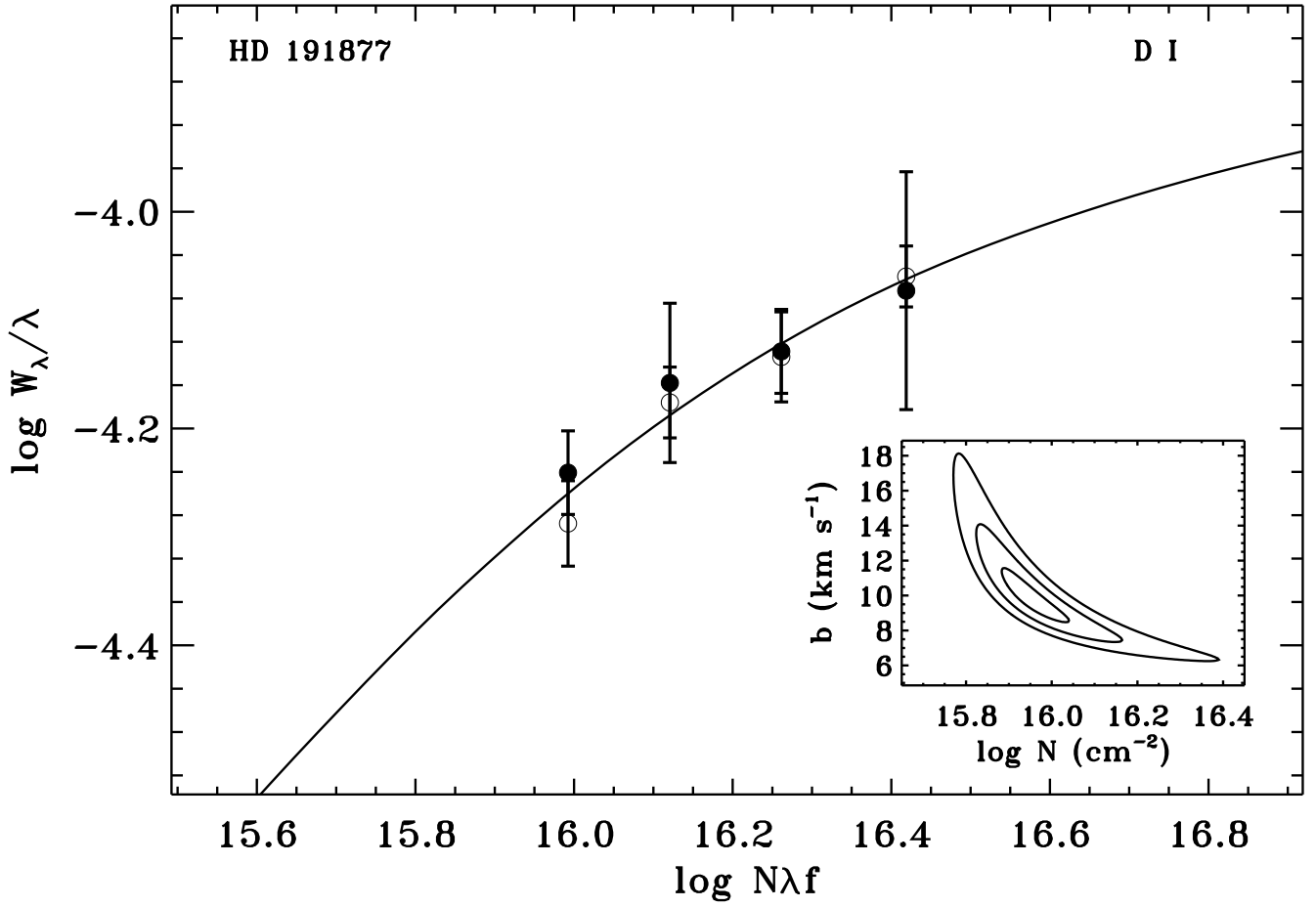


FIG. 9.— The best fit single-component curve of growth for D I toward HD 191877, which gives $\log N(\text{D I})=15.95\pm_{0.12}^{0.21}$ (2σ) and $b = 9.9\pm 4.0$ km s^{-1} (2σ). The filled circles are points measured from the SiC1 channel, and the open circles are points measured from the SiC2 channel. The inset shows a contour plot of the χ^2 distribution, with the 1σ , 2σ , and 3σ contours shown.

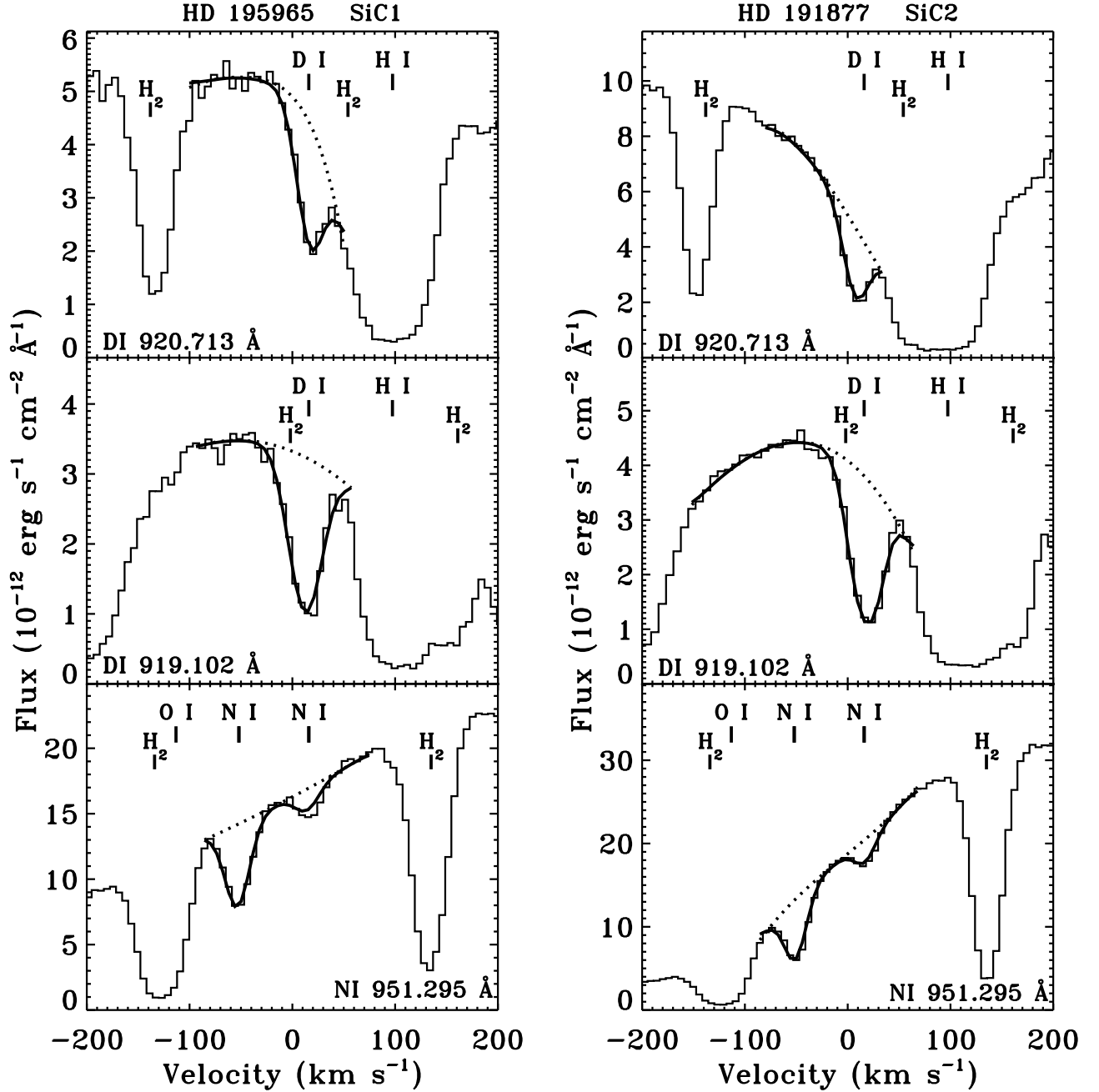


FIG. 10.— Examples of Owens-f absorption profile fits. The histogram lines are the data, the solid thick lines are the fits, and the dotted lines are the continua. Absorption features are labeled.

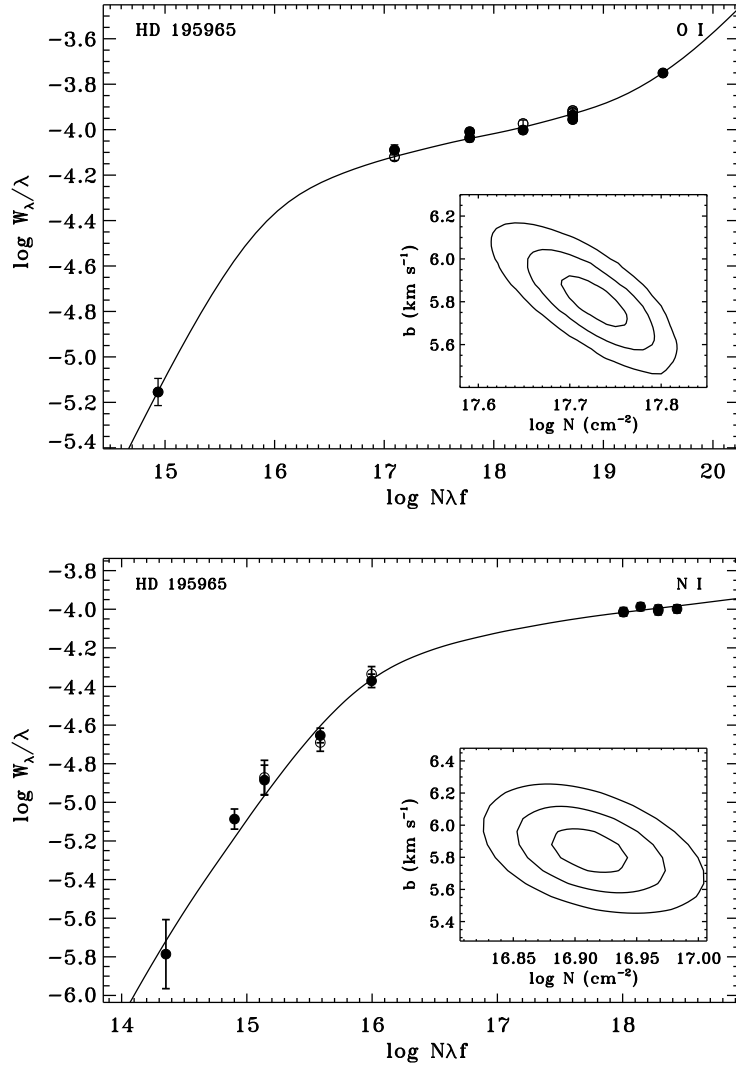


FIG. 11.— The best fit single-component curve of growth for O I (*top panel*) and N I (*bottom panel*) toward HD 195965. The COG parameters for O I are $\log N(\text{O I})=17.74\pm_{0.09}^{0.05}$ (2σ) and $b = 5.9 \pm 0.8 \text{ km s}^{-1}$ (2σ), and the parameters for N I are $\log N(\text{N I})=16.92\pm_{0.06}^{0.05}$ (2σ) and $b = 5.8 \pm 0.3 \text{ km s}^{-1}$ (2σ). The filled circles are points measured from either the *FUSE* SiC1 or LiF1 channel or from STIS, and the open circles are points measured from either the *FUSE* SiC2 or LiF2 channel. The insets show contour plots of the $\Delta\chi^2$ distributions, with the 1σ , 2σ , and 3σ contours shown.

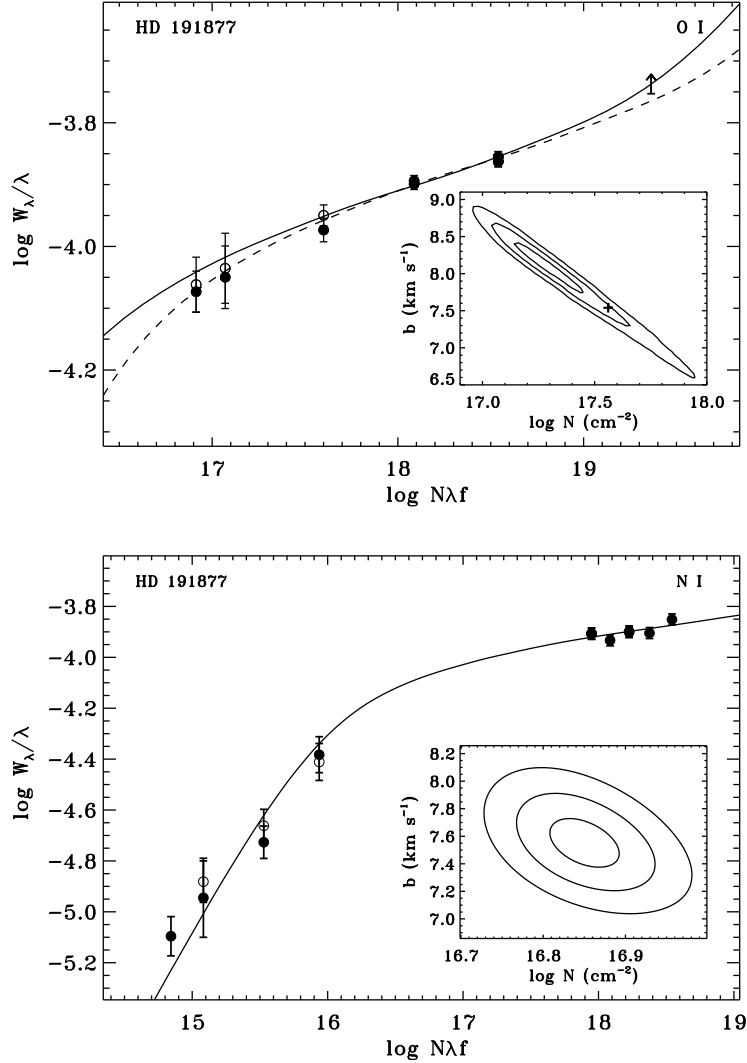


FIG. 12.— The best fit single-component curve of growth for O I (*top panel*) and N I (*bottom panel*) toward HD 191877. The COG parameters for O I are $\log N(\text{O I}) = 17.54 \pm_{0.12}^{0.20} \text{ cm}^{-2}$ (2σ) if b is forced to be 7.5 km s^{-1} as suggested by the N I COG (the COG for these parameters is shown as the solid line in the top panel). If b is allowed to vary, we find $\log N(\text{O I}) = 17.24 \pm_{0.22}^{0.42} \text{ cm}^{-2}$ (2σ) and $b = 8.2 \pm_{0.09}^{0.05} \text{ km s}^{-1}$ (2σ), the curve for which is shown as a dashed line in the top panel. The lower limit on the 1302.169 \AA line (the arrow in the top panel) restricts the O I column density to $\log N(\text{O I}) \geq 17.42 \text{ cm}^{-2}$. The parameters for N I are $\log N(\text{N I}) = 16.85 \pm_{0.08}^{0.08} \text{ cm}^{-2}$ (2σ) and $b = 7.5 \pm 0.5 \text{ km s}^{-1}$ (2σ). The filled circles are points measured from either the *FUSE* SiC1 or LiF1 channel, and the open circles are points measured from either the *FUSE* SiC2 or LiF2 channel. The insets show contour plots of the $\Delta\chi^2$ distributions, with the 1σ , 2σ , and 3σ contours shown. The plus sign in the inset for O I shows where b and N for the solid ($b = 7.5 \text{ km s}^{-1}$) COG fall on the $\Delta\chi^2$ contours. The large error bars for some O I equivalent widths are a result of continuum placement uncertainty.

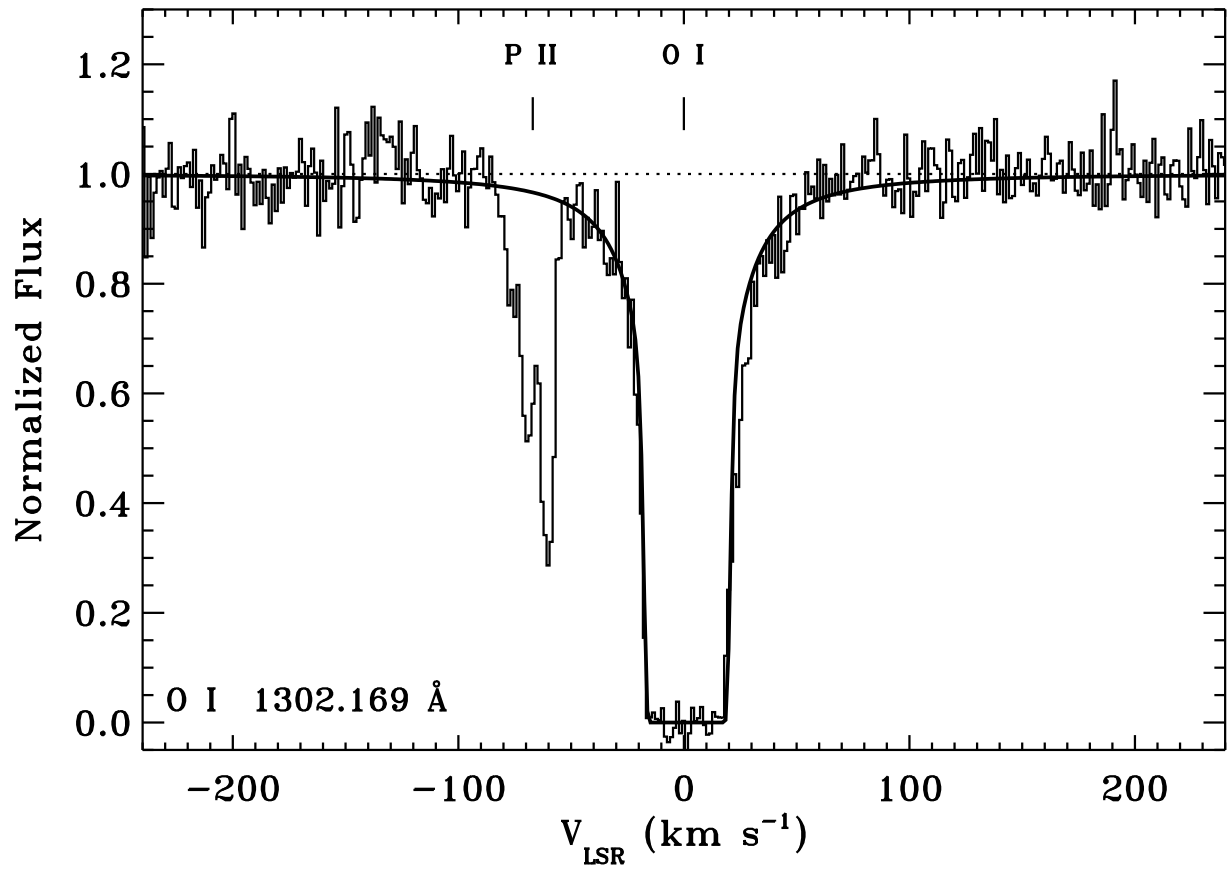


FIG. 13.— The continuum-normalized O I 1302.169 Å line profile from the STIS spectrum of HD 195965. A single-component model fit to the damping wings is also shown. The best fit model gives $\log N(\text{O I})=17.80$ and $b=6.3 \text{ km s}^{-1}$.

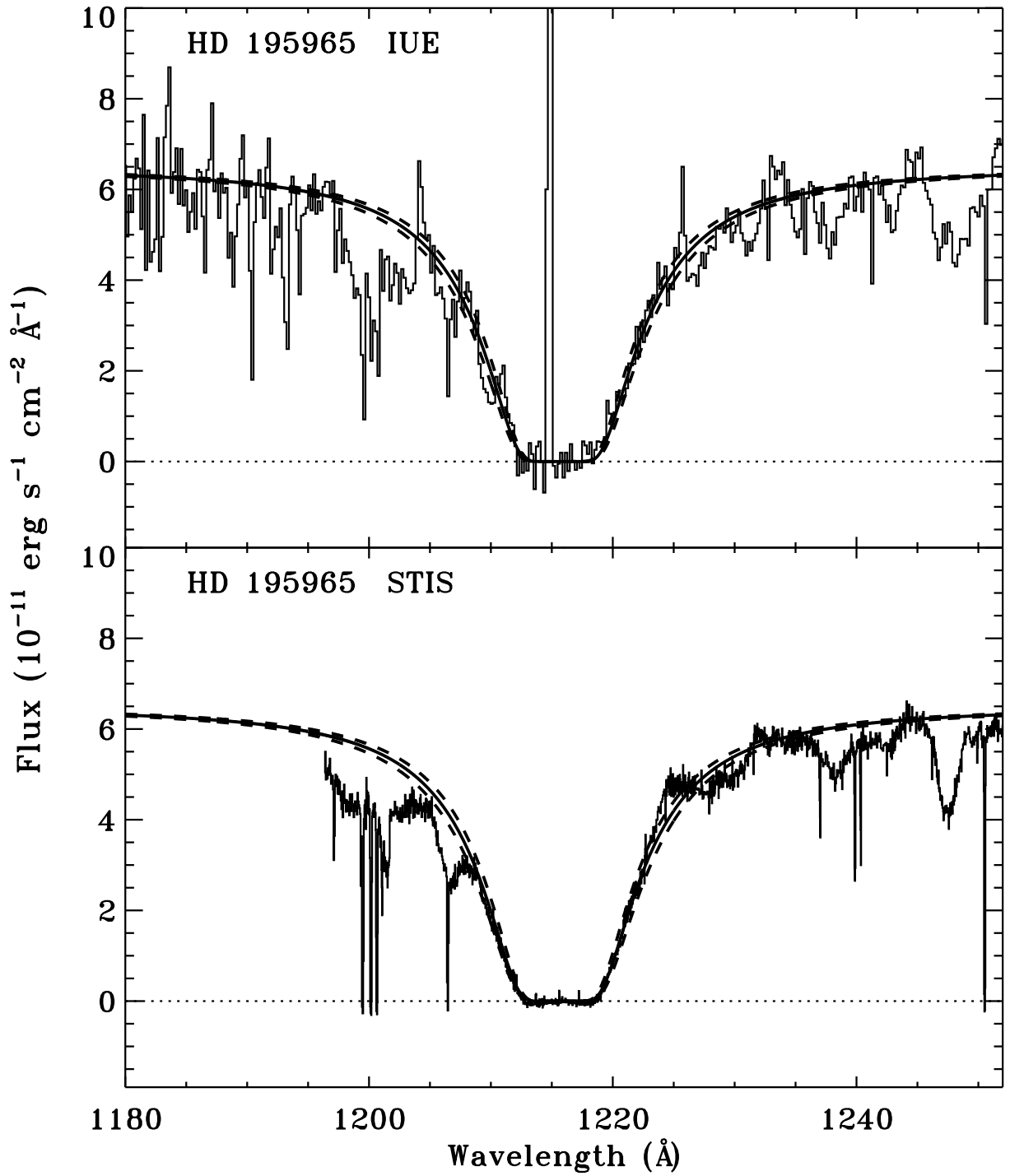


FIG. 14.— H I Ly α absorption toward HD 195965. The top panel shows small-aperture *IUE* data from Diplás & Savage (1994). The bottom panel shows the STIS spectrum. The best fit Voigt profile (solid line) and the $\pm 2\sigma$ profiles (dashed lines) are shown. The model shown is for $\log N(\text{H I}) = 20.95 \pm 0.05$.

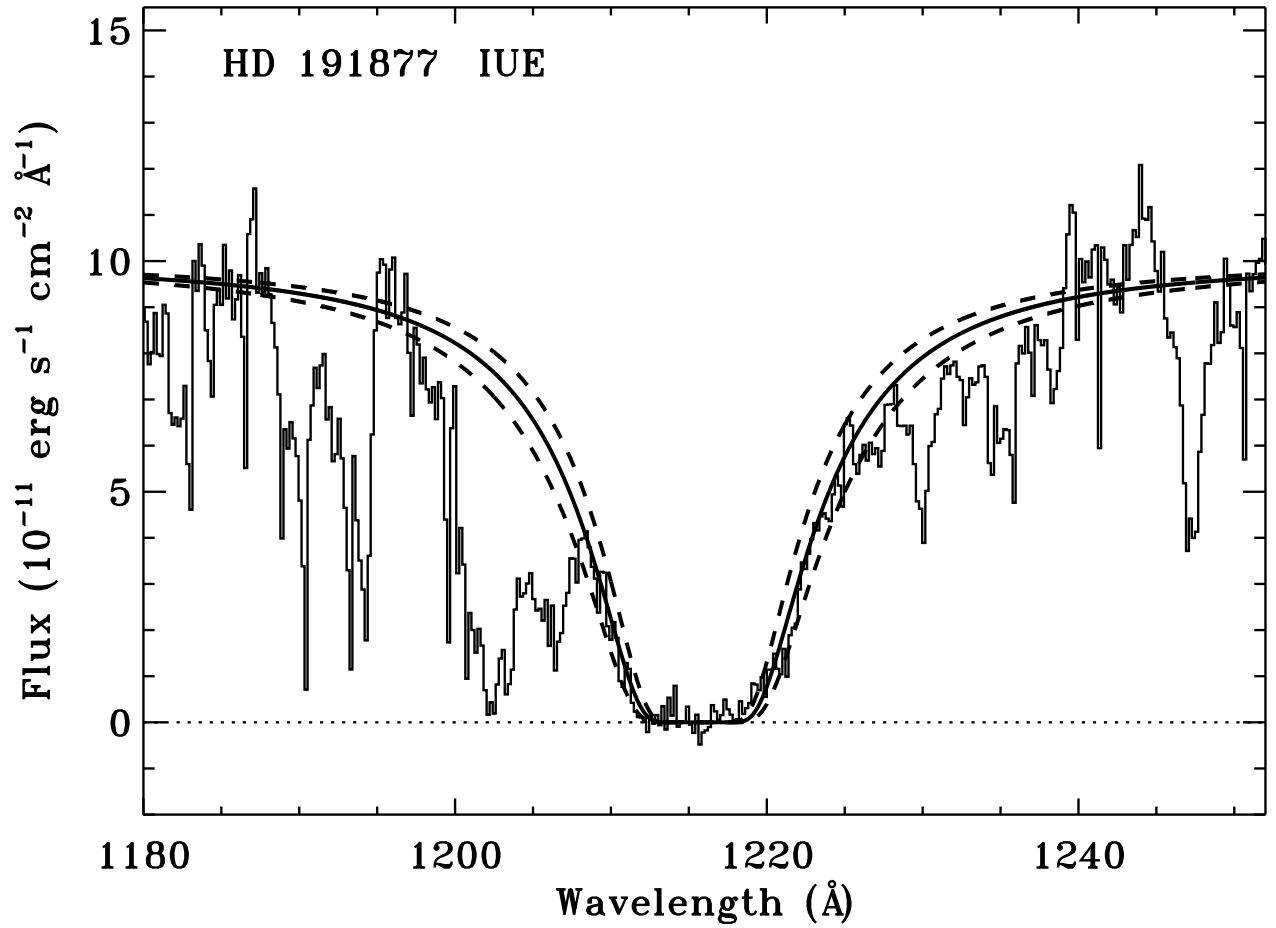


FIG. 15.— H I Ly α absorption toward HD 191877. The spectrum is small-aperture *IUE* data from Diplax & Savage (1994). The best fit Voigt profile (solid line) and the $\pm 2\sigma$ profiles (dashed lines) are shown. The model shown is for $\log N(\text{H I}) = 21.05 \pm 0.10$.

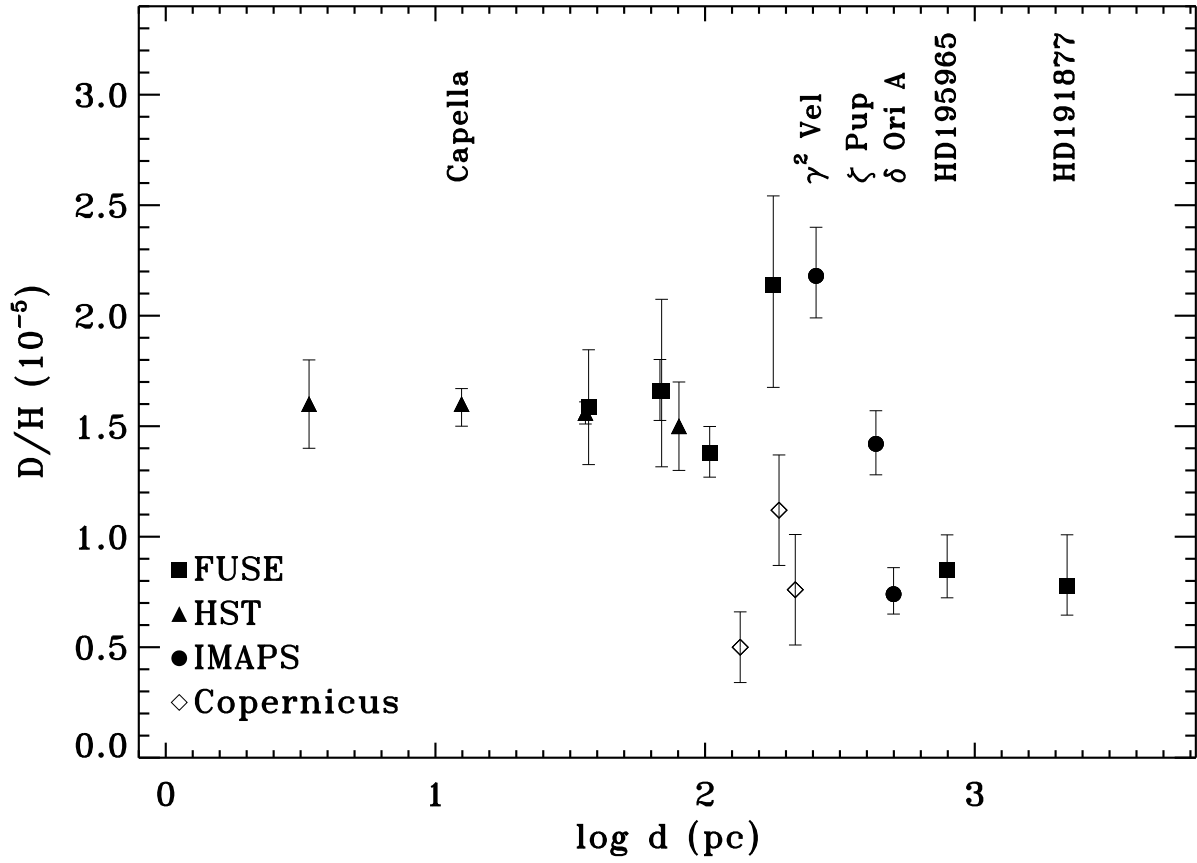


FIG. 16.— D/H measurements for 17 sight lines, plotted versus distance to the continuum source. The sight lines studied in this paper are labeled, as are the sight lines observed by *IMAPS* and the Capella sight line. Following Moos et al. (2002), the error bars shown are $2\sigma/2$. Adapted from Moos et al. (2002).

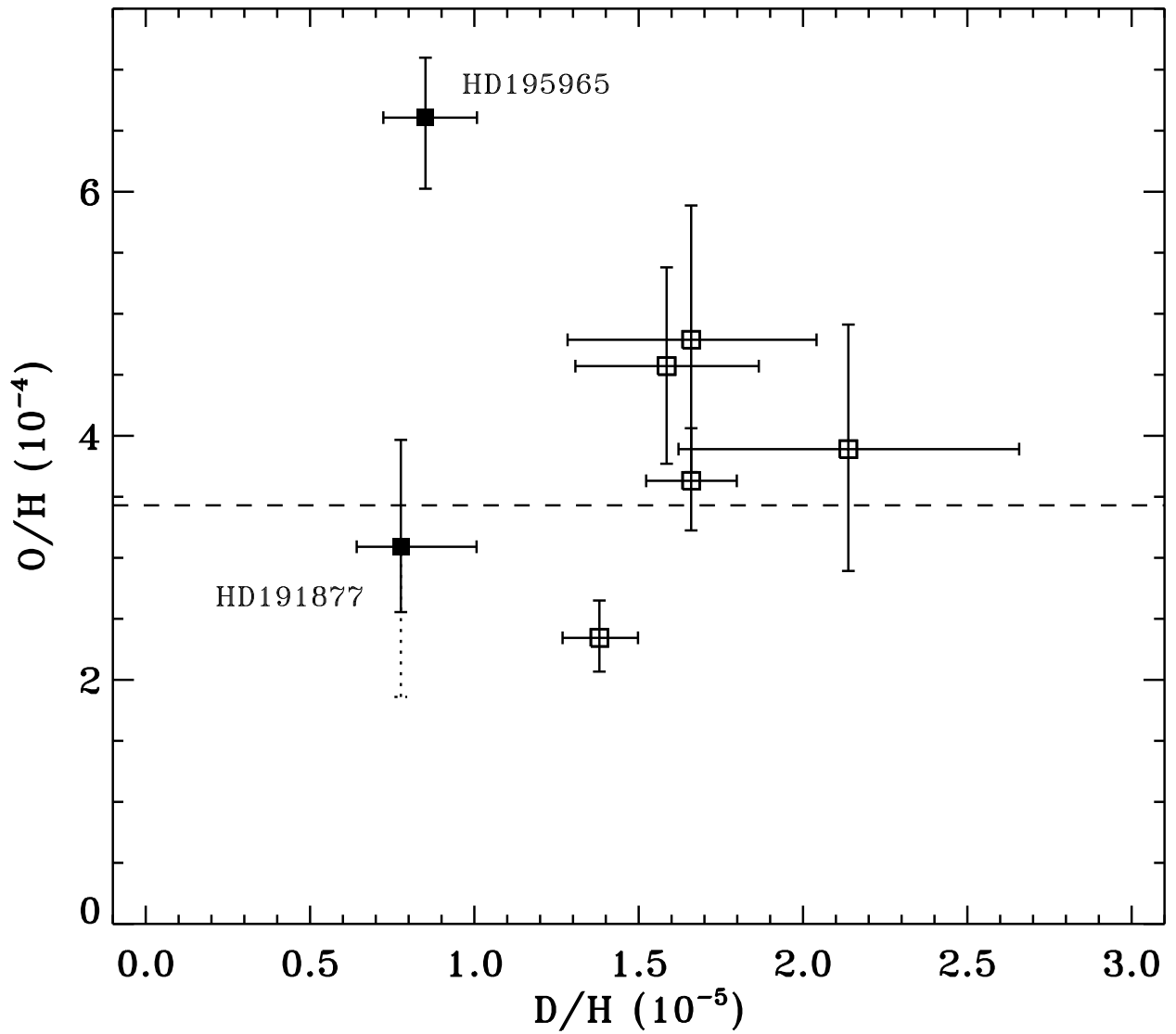


FIG. 17.— O I/H I for HD 195965, along with five of the seven original *FUSE* sight lines with reliable H I measurements (Moos et al. 2002). Following Moos et al. (2002), the error bars shown are $2\sigma/2$. The dashed line marks the O/H value found by Meyer et al. (1998) for the local ISM, corrected for the updated oscillator strength of the 1355.598 Å line (Meyer 2001). The dotted lower error bar on the HD 191877 point show the lower limit on O/H provided by the 1302.169 Å *IUE* measurement.

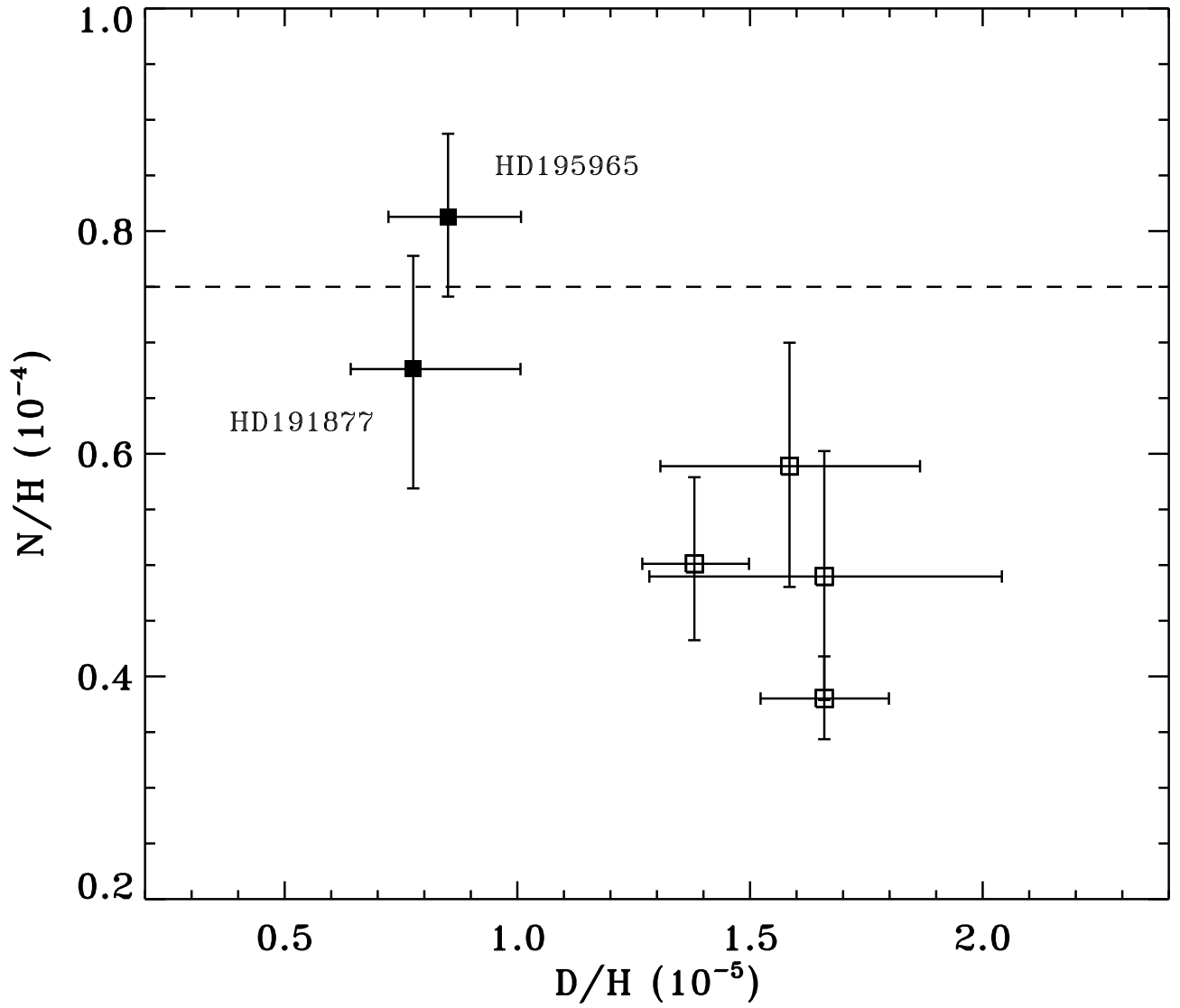


FIG. 18.— N I/H I for HD 195965 and HD 191877, along with four of the original *FUSE* sight lines (Moos et al. 2002) for which N/H could be determined. Following Moos et al. (2002), the error bars shown are $2\sigma/2$. The dashed line marks the N/H value found by Meyer et al. (1997) for the local ISM.

TABLE 1
SIGHT LINE INFORMATION^a

Name	HD 195965	HD 191877
l	85°71	61°57
b	5°00	-6°45
Distance ^b (pc)	794 ± 200	2200 ± 550
z dist. (pc)	69	-249
V (mag)	6.98	6.26
E(B-V)	0.25	0.18
Spectral Type	B0V	B1Ib
Log [N(HI) (cm ⁻²)] (<i>IUE</i>)	20.90 ± 0.09	20.90 ± 0.10

^aFrom Diplas & Savage (1994) and references therein.

^bWe have assumed 25% uncertainty associated with the spectroscopic parallax measurements.

TABLE 2
OBSERVATION LOG

Star	Instrument/Grating	Dataset ID	Observation Date	Exposure Time (s)	Aperture	λ coverage (\AA)
HD 195965	FUSE	P1028802, P1028803	2000 Nov 8,9	30000	LWRS	905 – 1187
HD 195965	FUSE	P1028801 ^a	2000 Jun 20	6400	LWRS	905 – 1187
HD 195965	STIS/E140H	O6BG01010	2001 Oct 9	415	$0.1'' \times 0.03''$	1197 – 1401
HD 195965	IUE	SWP10843	1980 Dec 20	1560	Small	1150 – 1970
HD 191877	FUSE	P2051101	2001 Jul 30	28100	LWRS	905 – 1187
HD 191877	FUSE	P1028701 ^a	2000 Jun 5	6100	LWRS	905 – 1187
HD 191877	IUE	SWP02837	1978 Oct 2	2280	Small	1150 – 1970

^aDatasets P1028701 and P1028801 were short snapshots. These data were included for the profile fitting analysis, but not for the curves of growth.

TABLE 3
INTERFERING LINES

λ (\AA)	Contaminating Lines
D I 972.272	H I Ly γ , O I λ 972.143
D I 949.484	H I Ly δ , H ₂ Lyman (14-0) P(2) λ 949.353, H ₂ Werner (3-0) P(2) λ 949.611
D I 937.548	H ₂ Werner (4-0) P(4) λ 937.557, Fe II λ 937.652
D I 930.495	O I λ 930.257, H ₂ Werner (4-0) R(2) λ 930.446, H ₂ Werner (4-0) Q(1) λ 930.578

TABLE 4
INTERFERING H₂ LINE REMOVAL PARAMETERS

D I λ (\AA)	ID	Interfering H ₂ λ (\AA)	$\log \lambda f^a$	ID	Template H ₂ λ (\AA)	$\log \lambda f^a$
919.102	Werner (5 – 0) R(4)	919.047	0.931	Lyman (13 – 0) R(4)	962.150	0.929
920.713	Werner (5 – 0) Q(4)	920.830	0.0678	Lyman (12 – 0) R(4)	970.830	0.194
922.900	Lyman (18 – 0) P(3)	922.893	-0.820	Lyman (17 – 0) R(4)	928.440	-0.511
925.974	none

^aOscillator strengths from Abgrall, Roueff, & Drira 2000.

TABLE 5
MEASURED EQUIVALENT WIDTHS TOWARD HD 195965

Wavelength (Å)	$\log \lambda f^a$	W_λ (SiC1 or LiF1) ^b (mÅ)	W_λ (SiC2 or LiF2) ^b (mÅ)
DI 919.102	0.0425	48.8 ± 3.9	38.4 ± 4.3
DI 920.713	0.171	54.9 ± 5.3	64.3 ± 8.4
DI 922.900	0.312	66.1 ± 12.2	74.2 ± 3.5
DI 925.974	0.469	77.4 ± 24.9	76.5 ± 10.2
OI 921.860	0.0402	84.9 ± 3.6	90.3 ± 3.4
OI 922.220	-0.646	75.1 ± 4.2	70.0 ± 2.7
OI 936.630	0.527	93.3 ± 3.6	99.6 ± 3.8
OI 1039.230	0.980	120.4 ± 4.6	126.1 ± 4.8
OI 1039.230	0.980	115.2 ± 4.4	123.5 ± 4.8
OI 1302.169 ^c	1.804	231.2 ± 5.9	...
OI 1355.598 ^c	-2.803	10.7 ± 2.1	...
NI 951.079	-0.911	40.5 ± 3.4	43.9 ± 4.1
NI 951.295	-1.766	12.4 ± 2.4	12.8 ± 2.9
NI 953.415	1.100	92.0 ± 4.4	92.6 ± 4.6
NI 953.655	1.377	93.6 ± 4.6	95.6 ± 4.6
NI 959.494	-1.321	21.3 ± 1.9	19.6 ± 2.2
NI 1134.165 ^d	1.237	116.9 ± 5.6	...
NI 1134.165 ^d	1.237	113.9 ± 5.6	...
NI 1159.817 ^d	-2.006	9.5 ± 1.2	...
NI 1160.937 ^d	-2.553	1.9 ± 1.0	...

^aOscillator strengths from Morton 1991, except that for the OI 1355.598 Å line, which is from Welty 1999.

^bLines with $\lambda < 1050$ Å were measured from the SiC spectra, and lines with $\lambda > 1000$ Å were measured from the LiF spectra.

^cThese measurements are from the STIS spectrum.

^dDetector x-walk effects due to the bright airglow lines at these wavelengths prevented the measurement of the line strengths in the LiF2 channel.

TABLE 6
MEASURED EQUIVALENT WIDTHS TOWARD HD 191877

Wavelength (Å)	$\log \lambda f^a$	W_λ (SiC1 or LiF1) ^b (mÅ)	W_λ (SiC2 or LiF2) ^b (mÅ)
DI 919.102	0.0425	52.8 ± 4.9	47.4 ± 4.5
DI 920.713	0.171	64.0 ± 11.8	61.4 ± 4.8
DI 922.900	0.312	68.6 ± 6.4	67.8 ± 6.8
DI 925.974	0.469	78.3 ± 22.5	80.7 ± 5.4
OI 921.860	0.0402	98.0 ± 4.4	103.5 ± 4.1
OI 922.220	-0.646	77.9 ± 6.2	80.0 ± 8.6
OI 925.446	-0.490	82.5 ± 10.2	85.3 ± 11.9
OI 936.630	0.527	119.6 ± 2.4	118.1 ± 2.4
OI 1039.230	0.980	145.0 ± 2.9	145.1 ± 2.9
OI 1039.230	0.980	142.6 ± 2.9	142.6 ± 2.9
NI 951.079	-0.911	39.4 ± 7.0	36.9 ± 6.7
NI 951.295	-1.766	10.8 ± 4.6	12.5 ± 2.6
NI 953.415	1.100	118.1 ± 6.2	118.1 ± 6.2
NI 953.655	1.377	120.6 ± 6.2	119.8 ± 6.2
NI 959.494	-2.006	18.0 ± 2.8	20.9 ± 3.4
NI 1159.817 ^c	-2.553	9.3 ± 1.8	...
NI 1134.165 ^c	1.237	132.2 ± 6.7	...
NI 1134.415 ^c	1.528	141.3 ± 7.2	...
NI 1134.980 ^c	1.693	159.8 ± 8.3	...

^aOscillator strengths from Morton 1991.

^bLines with $\lambda < 1050$ Å were measured from the SiC spectra, and lines with $\lambda > 1000$ Å were measured from the LiF spectra. The O I 1039 Å lines was measured in both LiF and SiC channels.

^cDetector x-walk effects due to the bright airglow lines at these wavelengths prevented the measurement of the line strengths in the LiF2 channel.

TABLE 7
COLUMN DENSITIES^a

Name	HD 195965			HD 191877		
	COG	Profile fit	Adopted Value ^b	COG	Profile fit	Adopted Value ^b
log N(D I)	15.83 $\pm_{0.11}^{0.14}$	15.97 $\pm_{0.13}^{0.13}$	15.88 $\pm_{0.13}^{0.14}$	15.95 $\pm_{0.12}^{0.21}$	15.93 $\pm_{0.11}^{0.19}$	15.94 $\pm_{0.12}^{0.21}$
log N(H I) ^c	...	20.95 ± 0.05	20.95 ± 0.05	...	21.05 ± 0.10	21.05 ± 0.10
log N(O I) ^d	17.74 $\pm_{0.09}^{0.05}$	17.80 $\pm_{0.09}^{0.05}$	17.77 $\pm_{0.09}^{0.04}$	17.54 $\pm_{0.08}^{0.20e}$...	17.54 $\pm_{0.08}^{0.20e}$
log N(N I)	16.92 $\pm_{0.06}^{0.09}$	16.83 $\pm_{0.04}^{0.09}$	16.85 $\pm_{0.06}^{0.09}$	16.85 $\pm_{0.08}^{0.08}$	16.93 $\pm_{0.10}^{0.07}$	16.88 $\pm_{0.10}^{0.08}$

^aError bars are 2σ estimates (95% confidence). For all of the adopted values except O I the uncertainties were chosen to be the largest uncertainties of the individual values, because the two measurements were made on the same data and are therefore not independent. For O I toward HD 195965 the measurements are largely independent, so the errors were added in quadrature.

^bFor D I and N I, the adopted value is the weighted mean of the single-component curve of growth and profile fitting results. When only one method was available (*e.g.*, H I), the result from that method is the adopted value.

^cThe H I column densities were derived by model fits to the damping wings of Ly α . For HD 195965, Ly α was observed with STIS, and for HD 191877 we reanalyzed *IUE* data from Diplas & Savage 1994.

^dThe O I column density toward HD 195965 was derived by a single-component curve of growth and a model fit to the damping wings of the 1302.169 Å line in the STIS data.

^eThe O I column density listed in the table is the value derived when b is set to 7.5 km s⁻¹. If b is allowed to vary, the best fit COG gives $\log N(\text{O I})=17.24\pm_{0.22}^{0.42}$ cm⁻² (see discussion in § 5).

TABLE 8
COLUMN DENSITY RATIOS^a

Name	HD 195965	HD 191877	Local ISM ^b
D/H	$(0.85 \pm_{0.24}^{0.34}) \times 10^{-5}$	$(0.78 \pm_{0.25}^{0.52}) \times 10^{-5}$	$(1.52 \pm 0.15) \times 10^{-5}$
D/O	$(1.29 \pm_{0.37}^{0.51}) \times 10^{-2}$	$(2.51 \pm_{0.86}^{2.14}) \times 10^{-2c}$	$(3.99 \pm 0.38) \times 10^{-2}$
D/N	$(1.07 \pm_{0.31}^{0.45}) \times 10^{-1}$	$(1.15 \pm_{0.36}^{0.75}) \times 10^{-1}$	$(3.30 \pm 0.40) \times 10^{-1}$
O/H	$(6.61 \pm_{1.11}^{1.03}) \times 10^{-4}$	$(3.09 \pm_{0.98}^{1.98}) \times 10^{-4c}$	$(3.03 \pm 0.42) \times 10^{-4}$
N/H	$(7.94 \pm_{1.34}^{1.69}) \times 10^{-5}$	$(6.76 \pm_{1.97}^{2.22}) \times 10^{-5}$	$(4.24 \pm 0.62) \times 10^{-5}$
O/N	$8.32 \pm_{1.52}^{1.66}$	$4.57 \pm_{1.45}^{2.83}$	8.1 ± 0.8

^aError bars are 2σ estimates (95% confidence).

^bMean Local ISM values from Moos et al. 2002 and references therein. The uncertainties for these values are 2σ in the mean.

^cThe D/O and O/H ratios toward HD 191877 listed in the table use the O I column density found by setting b to 7.5 km s^{-1} . If b is allowed to vary, we find $\text{D/O} = (5.01 \pm_{2.33}^{8.74}) \times 10^{-2}$, $\text{O/H} = (1.55 \pm_{0.69}^{2.56}) \times 10^{-4}$ (see discussion in § 5).